

University of Nebraska - Lincoln

DigitalCommons@University of Nebraska - Lincoln

---

Theses, Dissertations, and Student Research from  
Electrical & Computer Engineering

Electrical & Computer Engineering, Department of

---


12-2013

# FEA ESTIMATION AND EXPERIMENTAL VALIDATION OF SOLID ROTOR AND MAGNET EDDY CURRENT LOSS IN SINGLE-SIDED AXIAL FLUX PERMANENT MAGNET MACHINES

Xu Yang

University of Nebraska-Lincoln, xu.yang@huskers.unl.edu

Follow this and additional works at: <https://digitalcommons.unl.edu/elecengtheses>

 Part of the [Electrical and Electronics Commons](#), [Electromagnetics and Photonics Commons](#), and the [Power and Energy Commons](#)

---

Yang, Xu, "FEA ESTIMATION AND EXPERIMENTAL VALIDATION OF SOLID ROTOR AND MAGNET EDDY CURRENT LOSS IN SINGLE-SIDED AXIAL FLUX PERMANENT MAGNET MACHINES" (2013). *Theses, Dissertations, and Student Research from Electrical & Computer Engineering*. 66.  
<https://digitalcommons.unl.edu/elecengtheses/66>

This Article is brought to you for free and open access by the Electrical & Computer Engineering, Department of at DigitalCommons@University of Nebraska - Lincoln. It has been accepted for inclusion in Theses, Dissertations, and Student Research from Electrical & Computer Engineering by an authorized administrator of DigitalCommons@University of Nebraska - Lincoln.

FEA ESTIMATION AND EXPERIMENTAL VALIDATION OF SOLID ROTOR  
AND MAGNET EDDY CURRENT LOSS IN SINGLE-SIDED AXIAL FLUX  
PERMANENT MAGNET MACHINES

by

Xu Yang

A DISSERTATION

Presented to the Faculty of

The Graduate College at the University of Nebraska

In Partial Fulfilment of Requirements

For the Degree of Doctor of Philosophy

Major: Electrical Engineering

Under the Supervision of Professors Jerry Hudgins and Dean Patterson

Lincoln, Nebraska

December, 2013

FEA ESTIMATION AND EXPERIMENTAL VALIDATION OF SOLID ROTOR  
AND MAGNET EDDY CURRENT LOSS IN SINGLE-SIDED AXIAL FLUX  
PERMANENT MAGNET MACHINES

Xu Yang, Ph. D.

University of Nebraska, 2013

Advisors: Dean Patterson and Jerry Hudgins

The rotor and magnet loss in single-sided axial flux permanent magnet (AFPM) machines with non-overlapped windings is studied in this dissertation. Finite element analysis (FEA) estimations of the loss are carried out using both 2D and 3D modeling. The rotor and magnet losses are determined separately for stator slot passing and MMF space harmonics from currents in the stator. The segregation of loss between the solid rotor plate and the magnet is addressed. The eddy current loss reduction by magnet segmentation is discussed as well. Two prototype 24 slot/22 pole single-sided AFPMs, fabricated with both single layer (SL) and double layer (DL) windings are assembled. Methods of loss segregation are illustrated in order to separate the eddy current loss. Finally, an optimal design approach to axial flux permanent magnet machines is presented.

## ACKNOWLEDGMENTS

I would like to express my gratitude to my advisors, Dr Dean Patterson and Dr Jerry Hudgins for their support during my PhD. Their creative and critical thinking inspired me a lot during my research. I would never have been able to finish my PhD without their guidance and encouragement.

I would like to thank my committee members, Dr Sohrab Asgarpour and Dr Axel Enders for their suggestions and advice.

My sincere thanks James, Mark, John from the ME shop, and Dustin Dam for their work and help during the machine tests.

I would like to thank my fellow labmates, Fabio, Tanya, Jessica, Taesic and all others for their discussion and help. I would also thank my friends, Jiangchao, Jie, Qianqian for their kind help.

Last but not the least, I would like to thank my parents for their continuous support throughout my life.

# Contents

|   |            |
|---|------------|
| <b>Contents</b>   | <b>iv</b>  |
| <b>List of Figures</b>  | <b>ix</b>  |
| <b>List of Tables</b>   | <b>xii</b> |
| <b>1 Introduction</b>   | <b>1</b>   |
| 1.1 Motivation . . . . .  | 1          |
| 1.2 Literature Review . . . . .   | 2          |
| 1.2.1 Literature Review of Eddy Current Loss Analysis in Rotor and<br>Magnets . . . . . | 2          |
| 1.2.2 Literature Review of Stator Core Loss Analysis . . . . .                          | 4          |
| 1.2.3 Literature Review of Machine Design Optimization . . . . .                        | 6          |
| 1.3 Research Summary and Relevant Publications . . . . .                                | 8          |
| <b>2 Finite Element Analysis Simulations</b>  | <b>10</b>  |
| 2.1 Introduction . . . . .  | 10         |
| 2.2 Eddy Current Loss Analysis in Machines . . . . .                                    | 11         |
| 2.2.1 Eddy Current Loss due to Stator Slotting $P_{r,Slot}$ . . . . .                   | 11         |
| 2.2.2 Eddy Current Loss due to MMF Space Harmonics $P_{r,NOW}$ . . . . .                | 11         |

|          |   |           |
|----------|---|-----------|
| 2.3      | Machine Description . . . . .   | 12        |
| 2.4      | FEA Modeling . . . . .  | 13        |
| 2.4.1    | 2D FEA Model . . . . .  | 13        |
| 2.4.2    | 3D FEA Model . . . . .  | 14        |
| 2.4.3    | Eddy Current Loss Calculation in 2D and 3D FEA . . . . .                      | 15        |
| 2.4.3.1  | 2D and 3D Simulation Results Comparisons . . . . .                            | 16        |
| 2.5      | 3D FEA Simulations Results . . . . .  | 16        |
| 2.5.1    | Simulation Procedure . . . . .  | 16        |
| 2.5.2    | Eddy Current Loss Due to Stator Slotting and MMF Space<br>Harmonics . . . . . | 18        |
| 2.5.2.1  | Eddy Current Loss Due to Stator Slotting $P_{r,Slot}$ . . . . .               | 18        |
| 2.5.2.2  | Eddy Current Loss Due to MMF Space Harmonics<br>$P_{r,NOV}$ . . . . .         | 19        |
| 2.5.3    | Eddy Current Loss Separation in Solid Rotor Plate and Magnets                 | 19        |
| 2.5.4    | Eddy Current Loss Reduction in Split Magnets . . . . .                        | 21        |
| 2.5.5    | Eddy Current Loss on Various Speeds and Load Conditions . . . . .             | 23        |
| 2.5.5.1  | Eddy Current Loss on Speed Changes . . . . .                                  | 23        |
| 2.5.5.2  | Eddy Current Loss on Current Changes . . . . .                                | 24        |
| 2.5.6    | Conclusion . . . . .  | 24        |
| <b>3</b> | <b>Stator Core Loss Measurement</b>   | <b>25</b> |
| 3.1      | Introduction . . . . .  | 25        |
| 3.2      | Test Description and Schemes . . . . .  | 25        |
| 3.2.1    | Description of Test Stator Cores . . . . .                                    | 25        |
| 3.2.2    | Test Scheme . . . . .   | 26        |
| 3.3      | Core Loss Measurement in Unslotted Toroid . . . . .                           | 30        |

|          |  |           |
|----------|--|-----------|
| 3.3.1    | Test Verification at 60 Hz Compared with Steel Manufacturer's Data . . . . .     | 30        |
| 3.3.2    | Results at Frequencies (60 Hz, 100 Hz, 200 Hz, 300 Hz, 400 Hz, 500 Hz) . . . . . | 31        |
| 3.4      | Core Loss Measurement in Back Iron . . . . .                                     | 35        |
| 3.4.1    | FEA Simulations . . . . .  | 35        |
| 3.4.2    | Experimental Results . . . . .   | 36        |
| 3.5      | Core Loss Measurement in the Teeth . . . . .                                     | 39        |
| 3.5.1    | Method 1: Core Loss Measured at One Tooth Excited . . . . .                      | 39        |
| 3.5.1.1  | FEA Simulations . . . . .  | 39        |
| 3.5.1.2  | Experimental Results . . . . .   | 42        |
| 3.5.2    | Method 2: Core Loss Measured at One Phase (Four) Teeth Excited . . . . .         | 42        |
| 3.5.2.1  | FEA Simulations . . . . .  | 43        |
| 3.5.2.2  | Experimental Results . . . . .   | 44        |
| 3.5.3    | Method 3: Core Loss Measured at Three Phases (Twelve) Teeth Excited . . . . .    | 45        |
| 3.5.3.1  | FEA Simulations . . . . .  | 45        |
| 3.5.3.2  | Experimental Results . . . . .   | 46        |
| 3.5.4    | Comparison of Teeth Loss Results by the Three Methods . . . . .                  | 47        |
| 3.6      | Conclusion . . . . .   | 47        |
| <b>4</b> | <b>Experiment Verification</b>   | <b>49</b> |
| 4.1      | Introduction . . . . .   | 49        |
| 4.2      | Assembling of the Single-Sided AFPMs . . . . .                                   | 49        |
| 4.3      | Machine Parameters . . . . .   | 52        |

|          |  |           |
|----------|--|-----------|
| 4.3.1    | Back EMF Constant . . . . .  | 52        |
| 4.3.2    | Resistance . . . . .   | 53        |
| 4.4      | Test Setup . . . . .   | 53        |
| 4.5      | Loss Analysis of the AFPM Machines . . . . .   | 54        |
| 4.6      | Description of Tests . . . . .   | 54        |
| 4.6.1    | Test 1: Isolate the Bearing Friction Loss . . . . .  | 54        |
| 4.6.2    | Test 2: Isolate the Stator Core Loss . . . . .   | 57        |
| 4.6.3    | Test 3: No Load Tests . . . . .  | 57        |
| 4.6.4    | Test 4: Load Test . . . . .  | 59        |
| 4.6.4.1  | Double Layer Winding . . . . .   | 59        |
| 4.6.4.2  | Single Layer Winding . . . . .   | 60        |
| 4.6.5    | Comparison of the Eddy Current Loss Experiment Results and<br>FEA Simulation Results . . . . . | 61        |
| 4.7      | Summary and Possible Future Work . . . . .   | 61        |
| <b>5</b> | <b>Optimal Design of an Axial Flux PM Machine</b>  | <b>63</b> |
| 5.1      | Introduction . . . . .   | 63        |
| 5.2      | FEA Model of the Machine . . . . .   | 64        |
| 5.3      | Design Variables . . . . .   | 64        |
| 5.4      | Design Constrains . . . . .  | 65        |
| 5.5      | Design Objectives . . . . .  | 65        |
| 5.6      | Optimization Process . . . . .   | 66        |
| 5.7      | Optimization Results . . . . .   | 67        |
| 5.7.1    | Compare with Initial Design . . . . .  | 67        |
| 5.7.2    | Parameter Profile . . . . .  | 68        |
| 5.7.3    | Discussions . . . . .  | 70        |



|                                    |           |
|------------------------------------|-----------|
| 5.8 Summary . . . . .              | 71        |
| <b>6 Summary and Continue Work</b> | <b>72</b> |
| <b>Bibliography</b>                | <b>74</b> |

# List of Figures

|      |  |    |
|------|--|----|
| 2.1  | MMF space harmonic contents of a 24 slots/22 poles AFPM . . . . .                                      | 12 |
| 2.2  | The stators of the 24 slots/22 poles machine . . . . .   | 14 |
| 2.3  | FEA models . . . . .   | 15 |
| 2.4  | Eddy current paths . . . . .   | 16 |
| 2.5  | Fine meshing near the surface of the solid rotor plate . . . . .                                       | 17 |
| 2.6  | Eddy current loss $P_{r,Slot}$ due to stator slotting at zero current . . . . .                        | 18 |
| 2.7  | Eddy current loss $P_{r,NOW}$ due to MMF space harmonics at rated current<br>and rated speed . . . . . | 19 |
| 2.8  | Eddy current in solid rotor plate . . . . .  | 20 |
| 2.9  | Double layer windings time stepping simulation results at rated condition                              | 21 |
| 2.10 | Single layer windings time stepping simulation results at rated condition                              | 22 |
| 2.11 | Eddy current in non split and split magnets . . . . .  | 22 |
| 2.12 | Eddy current loss in single layer windings at rated current . . . . .                                  | 23 |
| 2.13 | Eddy current loss in double layer windings at rated current . . . . .                                  | 23 |
| 2.14 | Eddy current loss in single layer windings at rated speed . . . . .                                    | 24 |
| 2.15 | Eddy current loss in single layer windings at rated speed . . . . .                                    | 24 |
| 3.1  | Test scheme for core loss measurement . . . . .  | 26 |
| 3.2  | Test devices for core loss measurement . . . . .   | 27 |

- 3.3 Equivalent circuit of the tested toroid . . . . . 27
- 3.4 Unslotted toroid for core loss measurement . . . . . 30
- 3.5 M12-29G BH curves in unslotted toroid at 60 Hz . . . . . 31
- 3.6 M12-29G measured specific core loss in unslotted toroid at 60 Hz . . . . . 31
- 3.7 M12-29G BH loops at 60 Hz, 100 Hz, 200 Hz . . . . . 32
- 3.8 M12-29G BH loops at 300 Hz, 400 Hz, 500 Hz . . . . . 33
- 3.9 Experiment results for core loss measurement in unslotted toroid . . . . . 34
- 3.10 Core loss measurement in back iron . . . . . 35
- 3.11 FEA model for core loss measurement in back iron . . . . . 36
- 3.12 FEA results for core loss measurement in back iron . . . . . 37
- 3.13 Experiment results for core loss measurement in back iron . . . . . 38
- 3.14 Core loss measurement at one tooth excited . . . . . 39
- 3.15 Air gap adjustment . . . . . 40
- 3.16 FEA results for core loss measurement at one tooth excited . . . . . 41
- 3.17 Experiment results for core loss measurement at one tooth excited . . . . . 42
- 3.18 FEA results for core loss measurement at one phase (four) teeth excited . . . . . 43
- 3.19 Secondary voltages of different teeth at one phase (four) teeth excited . . . . . 44
- 3.20 Experiment results for core loss measurement at one phase (four) teeth  
excited . . . . . 44
- 3.21 FEA model at three phases (twelve) teeth excited . . . . . 45
- 3.22 Secondary voltages of different teeth at three phases (twelve) teeth excited . . . . . 46
  
- 4.1 Parts of the single-sided AFPM Machines . . . . . 50
- 4.2 Schematic drawings of the single-sided AFPM Machines . . . . . 51
- 4.3 Single-sided AFPM machines for experiment . . . . . 51
- 4.4 Single-sided AFPM machines for experiment . . . . . 52

|      |   |    |
|------|---|----|
| 4.5  | Single-sided AFPM machines for experiment . . . . .                     | 52 |
| 4.6  | Test setup . . . . .  | 53 |
| 4.7  | Equipments for the experiment . . . . .                                 | 55 |
| 4.8  | “Machine” with a uncut stator . . . . .                                 | 56 |
| 4.9  | Bearing and windage loss $P_{f+w}$ results . . . . .                    | 56 |
| 4.10 | Sensing coil in the stator . . . . .                                    | 57 |
| 4.11 | Sensing coil voltage at no load condition . . . . .                     | 58 |
| 4.12 | Loss seperation results at no load condition . . . . .                  | 58 |
| 4.13 | Test results for double layer winding at 6A (rms) . . . . .             | 59 |
| 4.14 | Loss seperation resutls for double layer winding at 6A (rms) . . . . .  | 60 |
| 4.15 | Test results for single layer winding at 6A (rms) . . . . .             | 60 |
| 4.16 | Loss seperation resutls for single layer winding at 6A (rms) . . . . .  | 61 |
| 5.1  | 2D FEA model of a single-sided double layer NOW 24 slots/ 22 poles AFPM | 64 |
| 5.2  | Flowchart of optimization with MATLAB/Maxwell . . . . .                 | 67 |
| 5.3  | Pareto front . . . . .  | 68 |
| 5.4  | Optimization results . . . . .  | 69 |
| 5.5  | Variables vs TorqueDensity . . . . .                                    | 69 |
| 5.6  | Variables vs Efficiency . . . . .                                       | 70 |

# List of Tables

|     |   |    |
|-----|---|----|
| 2.1 | Parameters of the Single-sided AFPM . . . . .   | 13 |
| 3.1 | Comparison of Measured Specific Core Loss Data at 60 Hz By Three<br>Methods . . . . . | 47 |
| 3.2 | Manipulated Measured Loss Data of M12-29G . . . . .                                   | 48 |
| 5.1 | Design Variables and Ranges . . . . .   | 64 |
| 5.2 | Design Constrains . . . . .   | 65 |
| 5.3 | Optimization Results . . . . .  | 68 |

# Chapter 1

## Introduction

### 1.1 Motivation

The development and design of electrical machines has changed over the last few decades due to materials and technology improvements. Axial flux permanent magnet (AFPM) machines have gained much attention because of their disc-shaped structure, which is suitable for traction systems such as in hybrid vehicles, and for use in wind power generation [1, 2, 3, 4, 5, 6, 7].

Fractional slot concentrated winding (FSCW) machines, with nonoverlapped windings (NOW), have also become attractive due to the short end-windings and consequently less copper loss, as well as their fault tolerance and flux weakening ability [8, 9, 10, 11, 12]. However, the rotor eddy current losses, which occur both in solid rotor and in magnets may increase dramatically, because of stator MMF space harmonics, and stator open slotting which is commonly used with form wound coils in AFPM machines.

A newly burgeoning research area - computer aided optimisation in machine design has been investigated during the last two decades coinciding with the increasing in

computing power to evaluate the performance of thousands of machine designs by 2D or 3D finite element analysis (FEA) models to minimize the losses or other design objectives.

This dissertation focuses mainly on the eddy current loss analysis in the rotor and magnets in single-side axial flux permanent machines. In the last, an optimal machine design approach is presented.

## **1.2 Literature Review**

### **1.2.1 Literature Review of Eddy Current Loss Analysis in Rotor and Magnets**

The estimation of rotor and magnet eddy current loss has been studied a lot recently [13]. There are basically two approaches to calculate the eddy current loss: using analytical methods and using finite element method in 2D or 3D modelling.

Bianchi (2007, 2010) [14, 15] provided a rapid estimation of rotor losses for choosing different combinations of slots and poles in the early stage of design. In [16, 17], the impact of MMF space harmonics is analysed based on a non slotted straight line model. In [3, 4, 18], the rotor losses are measured in an AFPM machine.

Polinder (2006, 2007) [19, 20] presents an analytical method to calculate the eddy current loss in rotor back iron. First, the flux density in the air gap due to stator current is determined. A Fourier series is then used to obtain the magnitudes of space harmonics of the flux density. The relative motion of the flux density harmonics is calculated. Based on the expressions derived by [21], the eddy current loss is calculated based on two-dimensional fields. Their later work that compares of the analytical method and the finite element calculation shows that analytical calculation

are overestimated or underestimated due to a number of assumptions [22, 23, 24]. The non-linear material properties and slot opening, which is not included in the calculation, have a major impact.

Extensive research has been conducted on the analytical calculation of the eddy current loss in magnets as in [25, 26, 27, 28], etc. Analytical 2-D modelling for predicting the eddy current loss in the permanent magnets due to the armature reaction field was proposed in Zhu (2001) [29], and later improved in [30, 31]. In [32], analytical estimation of the slotting effect on magnet loss is studied. In [33], a precise analytical calculation of rotor eddy current loss is developed. Different rotor layer material and dimensions are studied to reduce the eddy current loss. However, most of the analytical models are two-dimensional with simplifying assumptions. Complex equations are derived based on Maxwell equations.

A finite element model is preferred because its simulation is based on exact physical geometry, although it is time consuming. Two dimensional FEA is a common approach. Reference Ugalde (2010, 2011) [34, 35] analysed the eddy current loss in the solid rotor back iron and magnets in 2D time stepping FEA. It shows in general that single layer windings have higher losses than double layer winding and the loss in the solid back iron is higher than in magnets. In [36], the impact of rotor back iron resistivity on eddy current loss in rotor and in magnets is studied, which shows that the rotor back iron eddy current impact on the permanent magnet (PM) loss. In [16, 15], the impact of MMF harmonics of various orders on rotor loss is analyzed. They concluded that single layer windings have more rotor loss due the richer sub-harmonics than double layer windings. However, the use of a 2D model leads to an approximate result due to the limited radial extension of actual magnets and rotor in AFPM machines [6]. In [37], a hybrid calculation method, referred to as the finite-element aided analytical method, is presented to accurately predict the eddy loss in



AFPM machines. In [38], a hybrid approach using analytically 2D current sheet and 3D FEA is proposed for determining the eddy current loss in high speed PM rotors. In [39], a 3D finite element method that considered the harmonics of inverters is used to calculate loss in each part of the motor separately. It is proved that eddy current loss in permanent magnets from concentrated or NOW windings is larger than that from distributed windings.

### 1.2.2 Literature Review of Stator Core Loss Analysis

Core loss prediction and measurement has always been a concern for electrical machine design engineers especially because of the difficulty of quantifying increased core loss associated with increasing frequency. Steel manufacturers usually only provide 50/60 Hz core loss data, which is not sufficient for accurate core loss prediction at higher frequencies. The American Society of Testing and Materials (ASTM) and the International Electrotechnical Commission (IEC) set several standards for core loss measurements. Generally, there are three test fixtures used in industry: an Epstein frame, a toroid tester and a single sheet tester. In [40, 41, 42], the authors compare the results from these three testers. It is shown that higher core losses are obtained in a toroid tester compared to an Epstein frame, which is caused by the magnetic damage produced by shearing stresses in a toroid. The drawback of the single sheet tester is that the flux is only measured at the center of strips, which is the same defect as in the Epstein frame. The single sheet tester is the least popular and is mainly used for quality control. Thus the toroid tester, which approximates the machine's geometry is preferred by machine design engineers.

With the measured core loss data, a core loss model could be set up to estimate the stator core loss in a fabricated machine. Various core loss models have been

developed. Steinmetz did the early work since 1891 [43]. In classical equations, the core losses are separated into two parts: hysteresis and eddy current loss.

$$P = P_h + P_e = K_h f B_m^n + K_e f^2 B_m^2 \quad (1.1)$$

where,  $P_h$  is the hysteresis loss,  $P_e$  is the eddy current loss,  $K_h$  is the hysteresis loss coefficient,  $K_e$  is the eddy current loss coefficient,  $n$  is an empirically determined constant varying from 1.5 and 2.5, often taken as being equal to 1.6,  $f$  is the excitation frequency and  $B_m$  is the peak flux density.

Later research has added a third component called excess loss [44, 45], which explains the difference between experiment results and the two components above, shown as:

$$P = P_h + P_e + P_{ex} = K_h f B_m^2 + K_e f^2 B_m^2 + K_{ex} f^{1.5} B^{1.5} \quad (1.2)$$

where  $P_{ex}$  is the excess loss and  $K_{ex}$  is the excess loss coefficient. To summarize, hysteresis loss is the loss within the structure of the magnetic material at the domain level. Eddy current loss is the resistive loss due to induced electric current produced by the changing flux density. It is found that  $K_h$  is linked to material intrinsic properties and behaviour measured through permeability [42].  $K_e$  is assumed constant at lower frequencies .

$$K_e = \frac{K t^2}{\rho} \quad (1.3)$$

$K$  is the material determined constant,  $t$  is the material thickness, and  $\rho$  is the resistivity. However, at higher frequencies, (1.2) needs to be modified to take the skin effect into consideration.  $K_{ex}$  is found to vary with both frequency and flux density. In [46], the iron loss distribution is shown by a thermographic camera. It can be seen that at a lower speed, hysteresis loss is the main loss contributor, while at a higher

speed eddy current loss is responsible for the main loss.

Recent work, in Domeki (2004) [47], employs a step-wise approximation for core loss coefficients based on (2.1).  $K_h$  and  $n$  are different in certain peak flux density ranges. In Ionel (2006,2007) [48, 49] focuses on curve fitting of the Epstein data by variable coefficients. The model proposed based on (2.2) uses hysteresis loss coefficients, which are variable with frequency and induction, and eddy-current and excess loss coefficients, which are variable with induction only. These models are more accurate compared with the typical conventional core loss model with constant coefficients.

However, there is another concern that the measured core loss data produced by a toroid tester or by an Epstein frame are different from the actual fabricated stator core loss. The properties of steel in the fabricated stator will be changed during the manufacturing process Clerc(2012) [50]. Sprague(2012) [51] analyzes potential variations in the performance of the machine caused by the allowable variations of the magnetic properties of steel, such as eddy current loss differences due to thickness variation etc. Boglietti(2003) [52] shows that core loss increases due to the punching process, but that an annealing process allows removal of this increased core loss. Different lamination cutting techniques cause variations in losses and in permeability as presented by Arshad(2007), [53]. The electrical design engineer usually bypasses these problems by using corrective coefficients, known as "building or fabrication factors" based on the designers experience.

### **1.2.3 Literature Review of Machine Design Optimization**

The implementation of an optimization algorithm with analytical or FEA modelling in electrical machine design optimization has been studied recently. Genetic algorithm,

particle swarm optimization, and differential evolutions are generally used.

In [54, 55], the authors propose an analytical procedure for the design of a surface mounted PM machine with binary genetic algorithm in order to optimize a single objective function of material cost. In [56, 57], a multi-objective optimization of a 48 slot/4 pole interior permanent magnet (IPM) motor with three barriers per pole is presented. In [58], the optimization design of an IPM motor is presented by means of an FEA-based multi-objective genetic algorithm (MOGA). Three objectives are maximum torque, maximum constant power speed range and minimum torque ripple. In [59], the author includes rotor losses in the optimization process with an additional cost function.

There are some papers using particle swarm optimization in the machine design as in [60, 61, 62, 63, 64, 65]. In [60], a method of comparing three different machine types in terms of efficiency and weight using multi-objective PSO and 2D static FEA is presented. In [63] a transverse flux machine, in [62, 64] a switched reluctance machine and in [65] a surface mounted PM motor are discussed.

The implementation of a differential evolution in electrical machine design optimization has been studied recently. In [66, 67, 68, 69, 70, 71, 72, 73]. In [66], a multi-objective optimization for the design of an IPM motor based on the differential evolution and finite element model is presented. The objective is to minimize active volume and while maximizing the power output in the flux weakening area. In [67], an optimal design practice of an IPM machine with modular stator structure based on FEA and a differential evolution is discussed. Single and multi-objectives of maximum torque and minimum total harmonic distortion (THD) of back electromotive force (EMF) is implemented. In [68], an automated machine design process with differential evolution techniques is proposed to maximize the torque and efficiency. In [69, 70], a bi-objective optimization of a PM machine with 11 parameter variables

using computationally efficient-FEA and differential evolution are employed to minimize torque ripple and maximize the torque production per unit volume. In [71], a multi-objective optimization of a surface PM motor with five variables seeking the minimization of total weight and maximization of a goodness function, which is defined as torque per root square of losses at rated load is studied. The results obtained by using by differential evolution (DE) are compared with the response surface(RS) method. The paper shows DE has better capability for dealing with large number of candidate designs. In [72], an optimal design of a surface PM of with eight variables with the objective of relative cost of active materials is presented by differential evolution. Stopping criteria for DE algorithm are discussed based on the solution space and the design space.

### **1.3 Research Summary and Relevant Publications**

The scientific contribution of the work is summarized below:

Chapter 2 focuses on modeling of single-sided AFPM machines, especially simulations on the eddy current loss analysis in the solid rotor plate and magnets.

Chapter 3 focuses on the stator core loss measurement. Several methods are proposed to predict the stator core loss as accurately as possible, in order to separate the eddy current loss in machine testing experiments.

Chapter 4 focuses on the experiments of assembling, testing and loss segregation of the single-sided AFPM machines, and experimental verification of the eddy current loss and comparison with FEA results.

Chapter 5 proposes an optimal design approach to AFPM machines combined

with the Maxwell FEA model and MATLAB optimization algorithms.

Publications associated with this dissertation are:

1. X. Yang, Patterson, D., Hudgins, J., “Core Loss Measurement In a Fabricated Stator of a Single-sided Axial Flux Permanent Magnet Machine,” International Electric Machines and Drives Conference(IEMDC), 2013 IEEE , 12-15 May. 2013
2. X. Yang, Patterson, D., Hudgins, J., Colton,J.,”FEA Estimation and Experimental Validation of Solid Rotor and Magnet Eddy Current Loss in Single-sided Axial Flux Permanent Magnet Machines,” Energy Conversion Congress and Exposition (ECCE), 2013 IEEE , 16-20 Sep. 2013
3. X. Yang, Patterson, D., Hudgins, J., “Multi-Objective Design Optimization of a Single-sided Axial Flux Permanent Magnet Machine,” International Conference on Electrical Machines and Systems(ICEMS), 2013 IEEE , 26-29 Oct. 2013
4. X. Yang, Patterson, D., Hudgins, J., “Permanent magnet generator design and control for large wind turbines,” Power Electronics and Machines in Wind Applications (PEMWA), 2012 IEEE , vol., no., pp.1,5, 16-18 July 2012

# Chapter 2

## Finite Element Analysis Simulations

### 2.1 Introduction

The goal of this chapter is to analyze the eddy current loss in the solid rotor plate and in the magnets of a single-sided AFPM machine with NOW. FEA estimations of the loss are carried out using both 2D and 3D modeling. The rotor and magnet losses are determined separately for stator slot passing and MMF space harmonics from currents in the stator. The segregation of loss between the solid rotor plate and the magnet is addressed. The eddy current loss reduction by magnet segmentation is also discussed.

## 2.2 Eddy Current Loss Analysis in Machines

The machine power balance is as [74]:

$$P_m - P_e = P_{f+w} + P_{s,Cu} + P_{s,Fe} + P_{r,Slot} + P_{r,NOW} \quad (2.1)$$

where  $P_m$  is the input mechanical power,  $P_e$  is the output electrical power,  $P_{f+w}$  is the friction and windage loss,  $P_{s,Cu}$  is the stator copper loss,  $P_{s,Fe}$  is the stator iron loss,  $P_{r,Slot}$  is the eddy current loss (in both the solid rotor iron and magnets) caused by stator slotting(which is calculated and measured with no current in the windings),and  $P_{r,NOW}$  is the rotor and magnet eddy current loss due to MMF space harmonics caused by NOW. One goal of this paper is to determine separately the losses ( $P_{r,Slot}$  and  $P_{r,NOW}$ ). The eddy current loss due to pulse-width modulation(PWM)harmonics, is not considered in this dissertation.

### 2.2.1 Eddy Current Loss due to Stator Slotting $P_{r,Slot}$

There is flux density variation due to the stator slot opening, which induces eddy currents in the rotor iron and permanent magnets as well. It can be calculated or measured at no load conditions, i.e. when the input current is zero.

### 2.2.2 Eddy Current Loss due to MMF Space Harmonics

$$P_{r,NOW}$$

The NOW exhibit a rich spectrum of space harmonics in the air gap MMF distribution. Thus the rotor loss is caused by different orders of MMF harmonics which are asynchronous with the rotor, inducing current in both the rotor iron and magnets. The amplitude of the MMF harmonics can be computed by the star of slots



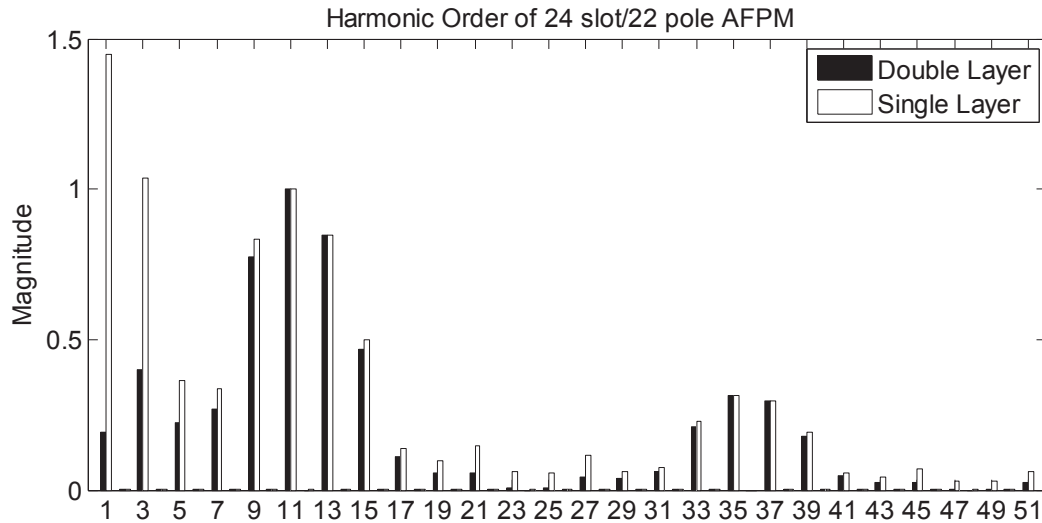


Figure 2.1: MMF space harmonic contents of a 24 slots/22 poles AFPM

theory [9, 10]. Fig. 2.1. shows the space harmonic contents of a 24 slot/22 pole starter MMF through Fourier analysis, with both single layer winding and double layer winding. The main space harmonic is on the order of 11. As is shown, in the single layer windings there are large magnitude subharmonics, which are harmonics lower than the main harmonic order. It is, therefore, expected that the rotor and magnet loss in single layer windings will be much higher than for the double layer windings.

## 2.3 Machine Description

The machine designed is to be used for the starter/alternator in a hybrid electric vehicle. The parameters of the 24 slot /22 pole single-sided AFPM machine are shown below in Table. I. Two mechanically identical machines were built, one with single layer winding and one with a double layer winding as shown in Fig. 2.2.

Table 2.1: Parameters of the Single-sided AFPM

|                                 |                         |
|---------------------------------|-------------------------|
| Rated power                     | 6.7 kW                  |
| Nominal speed                   | 2800 rpm                |
| Nominal torque                  | 23 Nm                   |
| Nominal current                 | 22.5A                   |
| Number of slots(Ns)             | 24                      |
| Number of poles(p)              | 22                      |
| Stator outer radius             | 98mm                    |
| Stator inner radius             | 58mm                    |
| Stator height                   | 45mm                    |
| Slot width                      | 8mm                     |
| Slot depth                      | 35mm                    |
| Stator back iron thickness      | 10mm                    |
| Rotor back iron thickness       | 6mm                     |
| Magnet thickness                | 4mm                     |
| Magnet pole arc                 | 14 deg                  |
| Turns per coil in SL            | 20                      |
| Turns per coil in DL            | 10                      |
| Stator steel type               | M12-29G                 |
| Rotor steel type                | mild steel              |
| Conductivity of rotor steel     | $6.99 \times 10^6$ S/m  |
| Magnet type                     | NdFeB-N40               |
| Remanence Br                    | 1.26 T                  |
| Relative permeability of magnet | 1.05                    |
| Conductivity of Magnet          | $0.625 \times 10^6$ S/m |

## 2.4 FEA Modeling

The FEA software is Ansoft Maxwell. A 2D FEA model is generally used to provide a quick calculation. A 3D FEA model is preferred to evaluate the detailed performances. In the FEA work, and the built machines, each pole is split radially into 2 equal segments, to control eddy current losses in the magnets.

### 2.4.1 2D FEA Model

The approach to modeling the AFPM in 2D is to view the machine from the side. The geometry is a cylindrical cross-section taken at an average radius as shown in Fig. 2.3.(b).

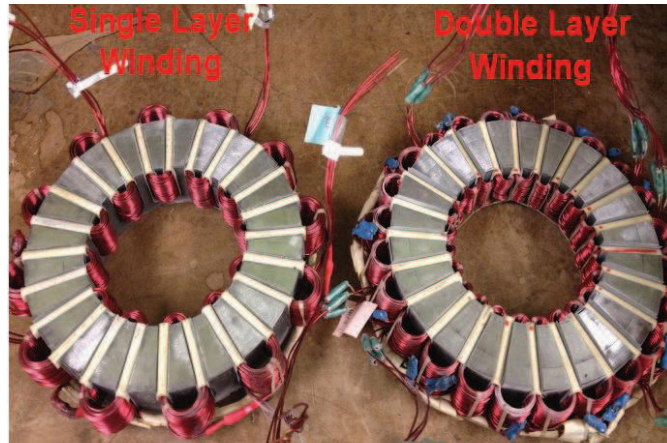


Figure 2.2: The stators of the 24 slots/22 poles machine

Rotational motion is assigned to the model as if it was a very small portion of a radial flux machine with a very large radius, for example 100 m, where the center of rotation is vertically above the drawings of Fig. 2.3. For the 24 slot/22 pole machine, only a very small fraction of the large radial flux machine is modeled. The symmetry multiplier in the FEA is however set to 2 with the master and slave boundary conditions applied. The model is shown in Fig. 2.3.(c).

### 2.4.2 3D FEA Model

The 3-D model is shown in Fig. 2.3.(d). It is expected that more accurate results will be obtained since the physical geometry is utilized, though it is time consuming. It is noticed that the torque calculation in FEA remains stable, but the rotor and magnet eddy current loss calculation is sensitive to solver parameters such as mesh, time step and nonlinear solver residual, which will be detailed later. .

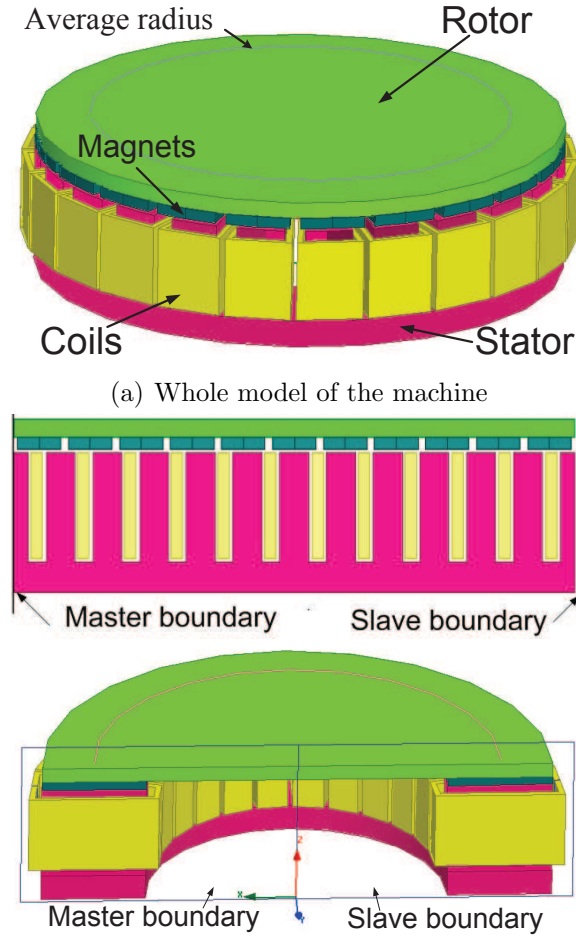


Figure 2.3: FEA models

### 2.4.3 Eddy Current Loss Calculation in 2D and 3D FEA

The algorithm used to calculate the eddy current loss is:

$$P_r = \frac{1}{\sigma} \int_{vol} J^2 dV \quad (2.2)$$

in which  $\sigma$  is the conductivity of the material,  $J$  is the current density,  $vol$  is the volume. In 2D FEA,  $J$  is the eddy current in the  $z$ -direction,  $P_r$  is calculated as the integral over the model surface and multiplied by the model depth in the  $z$ -direction. In 3-D FEA, it works out element by element the actual current distributions and directions in 3-D space. Thus it should be more accurate.

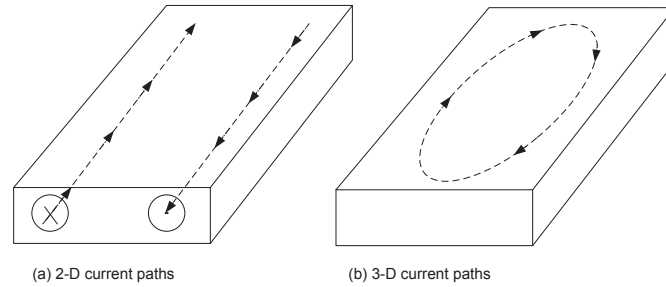


Figure 2.4: Eddy current paths

### 2.4.3.1 2D and 3D Simulation Results Comparisons

It can be seen that 2D and 3D FEA results differ a lot as seen later in Fig. 2.6. Since the 2-D FEA model's current is only in the Z direction, there are no end effects. Thus we expect the loss to be higher in 2D FEA. The 3D FEA should perform more accurately since it models the actual geometry. The simulation time takes about 10 to 20 hours. In contrast, 2D FEA takes less time, about 10 min, however, the value of the 2D results for application to a 3D machine is in doubt. Thus 3D FEA is implemented.

## 2.5 3D FEA Simulations Results

### 2.5.1 Simulation Procedure

In 3D FEA, meshing is critical. Skin effects need to be considered for the eddy current loss calculation. Now:

$$\delta = \sqrt{\frac{2\rho}{2\pi f \mu_0 \mu_r}} \quad (2.3)$$

in which,  $\delta$  is the skin depth,  $\rho$  is the material resistivity,  $f$  is the frequency,  $\mu_r$  is the relative permeability. The solid steel has a skin depth of 0.28 mm at 500 Hz. For the magnet, the NeFeB-N40 is 87 mm at 500 Hz. Thus a fine mesh is needed

near the solid rotor plate surface. In order to do that, two layers of skin sheets are created near the surface of the rotor plate for meshing. The meshing is illustrated as an example in Fig.2.5.

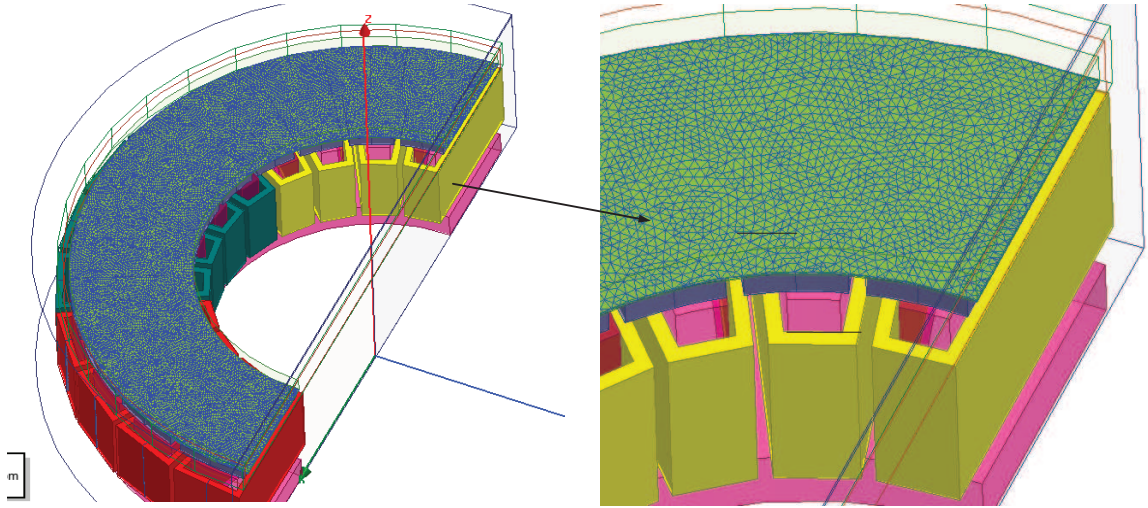


Figure 2.5: Fine meshing near the surface of the solid rotor plate

The mesh should not be too coarse or too fine. A good mesh is determined by trial and error. Too fine a mesh leads to unnecessary computation time, and can make the solution unstable.

The time step is also crucial. A large time step causes non physical answers. It was determined that a time step should be less than the time of one mechanical degree of rotation. In this simulation, the total number of mesh elements is around 215,205 tetrahedra, in the rotor, there are 143,870 tetrahedra, and the time step at 2800 rpm is 54 us. For a simulation time of 5 5ms, it takes 10 to 20 hours on an Intel(R) core(TM) i7-2600 CPU3.4 GHz computer with 16G RAM.

A no load simulation with zero stator current is conducted first. Then a loaded simulation with rated current is performed. The conductivity of the stator iron is set to zero, so that there is only eddy current loss in the solid rotor plate and in the permanent magnets. In separating the eddy current loss in the solid rotor plate only

from the total eddy current loss, the conductivity of the permanent magnets is set to zero and vice versa. In order to match the experiment results, the air gap is set to 1.78 mm, which is different to the original design of 1 mm.

Each simulation takes five electrical cycles. The simulation results are averaged at the last cycle to be more accurate.

## 2.5.2 Eddy Current Loss Due to Stator Slotting and MMF Space Harmonics

### 2.5.2.1 Eddy Current Loss Due to Stator Slotting $P_{r,Slot}$

The simulation is first conducted with no current in the stator windings at a range of speeds in order to determine the rotor plate and magnet loss due to stator slotting only.  $P_{r,Slot}$  is the same in both the single layer and double layer windings since the stator geometries are identical. As shown in Fig. 2.6,  $P_{r,Slot}$  is increased as the speed goes up.

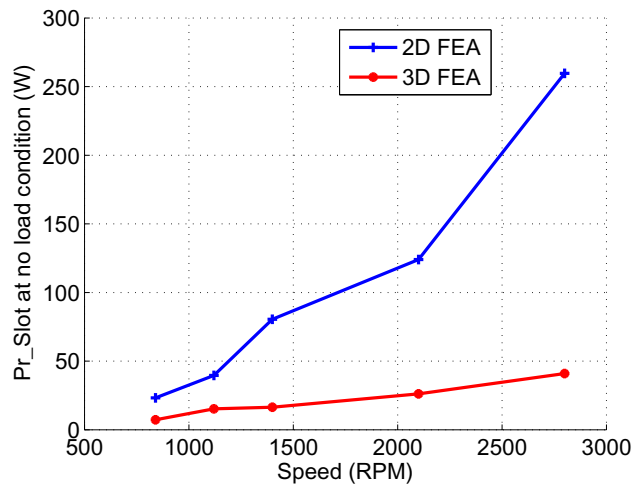


Figure 2.6: Eddy current loss  $P_{r,Slot}$  due to stator slotting at zero current

### 2.5.2.2 Eddy Current Loss Due to MMF Space Harmonics $P_{r,NOW}$

The same procedure is performed with a rated stator current to provide the rated torque for a range of rotor speeds.  $P_{r,NOW}$  is separated from the total loss by subtraction of the results of Fig. 2.6, as shown in Fig. 2.7. Here it is assumed that  $P_{r,NOW}$  remains the same at no load and loaded conditions in order to separate  $P_{r,NOW}$ . As can be seen, single layer windings produce more eddy current loss than double layer windings. With a double layer winding, at 2800 rpm, the eddy current loss due to stator slotting is 41 W, which is slightly higher than  $P_{r,NOW}$  which is 37.9 W. With a single layer winding, the major eddy current loss is due to MMF harmonics, at 2800 rpm, which is 113 W and accounts for 73.5% of total loss.

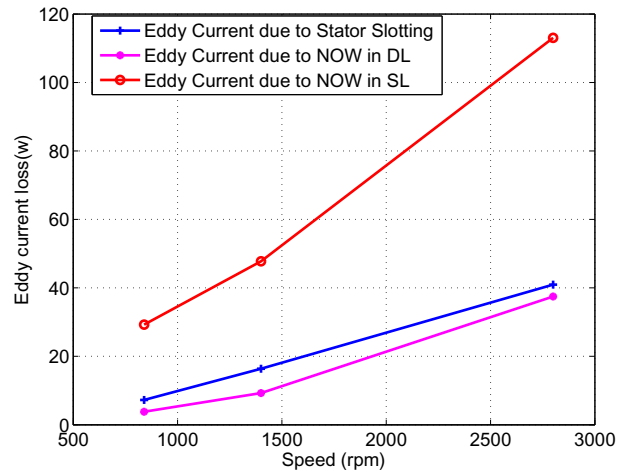
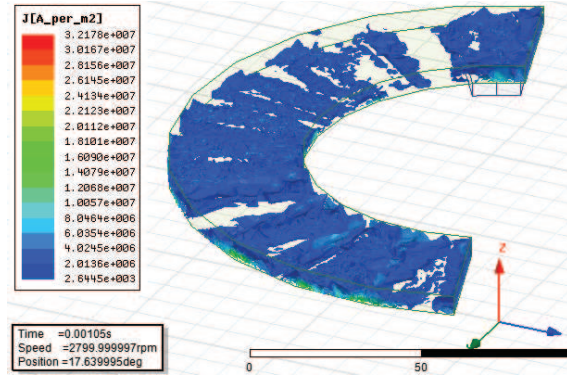


Figure 2.7: Eddy current loss  $P_{r,NOW}$  due to MMF space harmonics at rated current and rated speed

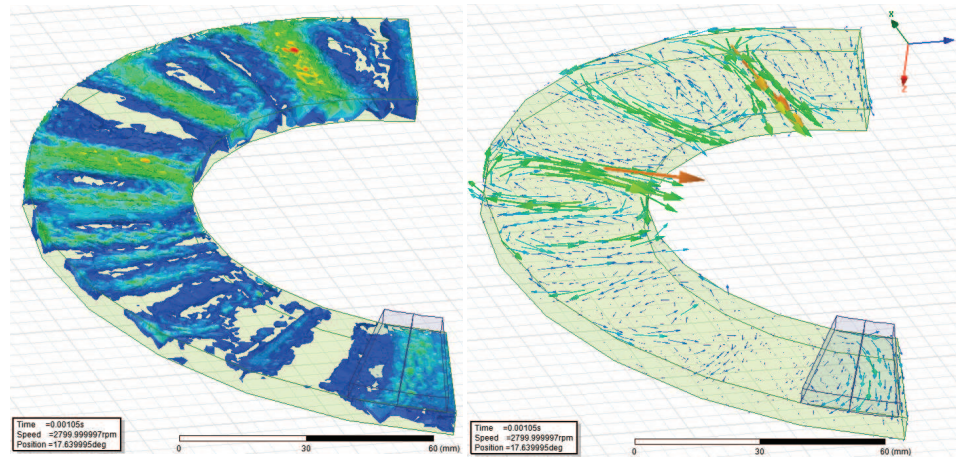
### 2.5.3 Eddy Current Loss Separation in Solid Rotor Plate and Magnets

In axial flux machines, a solid rotor plate is used because of mechanical integrity concerns. With a traditional distributed winding, a solid rotor back iron does not





(a) Eddy current in solid rotor plate



(b) Eddy current in solid rotor plate (view from flipping over)

Figure 2.8: Eddy current in solid rotor plate

experience a strong changing flux field as occurs in the stator steel. However in NOW, the large magnitude of stator MMF harmonics rotating asynchronously with the rotor will induce more eddy current loss in a solid rotor plate.

A 3D FEA model is implemented. To reduce the simulation time, the center of the rotor plate is subtracted. The eddy current distribution in the solid rotor plate is shown in Fig. 2.8(a). The current concentrates on the rotor lower surface due to skin effect. Fig. 2.8(b) provides a better view of the eddy current density and directions by flipping over the rotor plate.

Fig. 2.10 shows the eddy current loss separation results at rated current and rated

speed in single layer windings by 3 simulations. The total loss is about 151 W. The loss in the magnets only of 46 W, found by disabling eddy effects in the rotor plate, and the loss in rotor plate only, found similarly of about 110 W. The sum of the separated losses is slightly higher than the loss 151 W when eddy effects are enabled in both since eddy current in one object actually reduces the flux variations, and hence eddy current losses, in all adjacent conducting objects.

In Fig. 2.10, it can be seen that in the single layer windings, the eddy current loss in the rotor plate is a larger portion of the total loss, compared to double layer winding, due to high MMF sub harmonics.

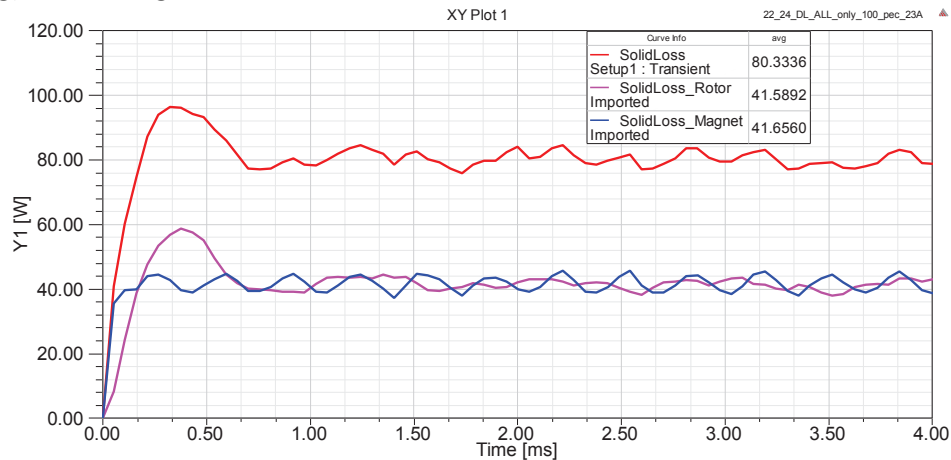


Figure 2.9: Double layer windings time stepping simulation results at rated condition

The solid rotor eddy current loss is larger than the magnet loss due to several reasons. The skin effect in the solid rotor plate impacts much more than in the magnets. Also, the magnets are split to reduce the loss while in the rotor plate, the conductive path is not restricted.

### 2.5.4 Eddy Current Loss Reduction in Split Magnets

In FEA and built machines, each pole is split radially into two equal segments, to control eddy current losses in the magnets. The eddy current density reduces in the

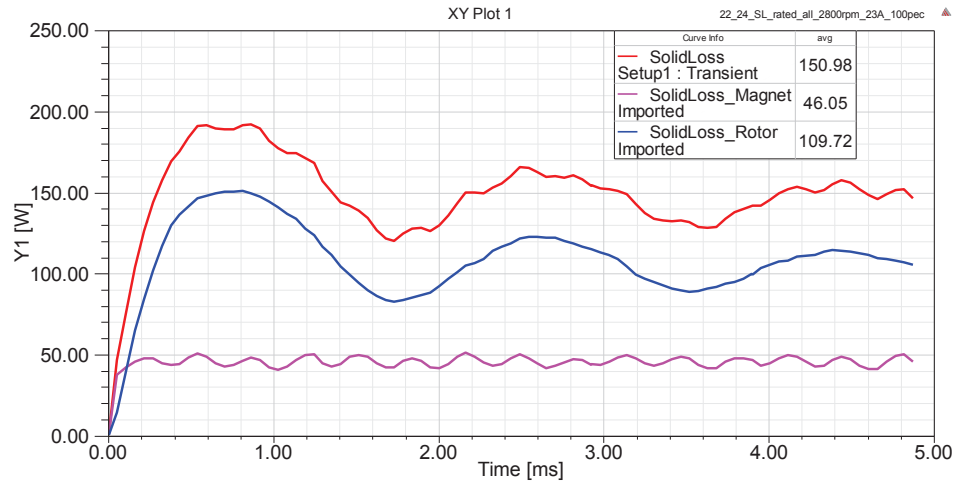


Figure 2.10: Single layer windings time stepping simulation results at rated condition split magnets, compared with non split magnets. The simulation results show that the eddy current loss in split magnets in single layer winding at rated current is 45.7 W , compared to non split magnets with 85 W eddy current loss, in splitting results in a loss with a reduction of 47 %.

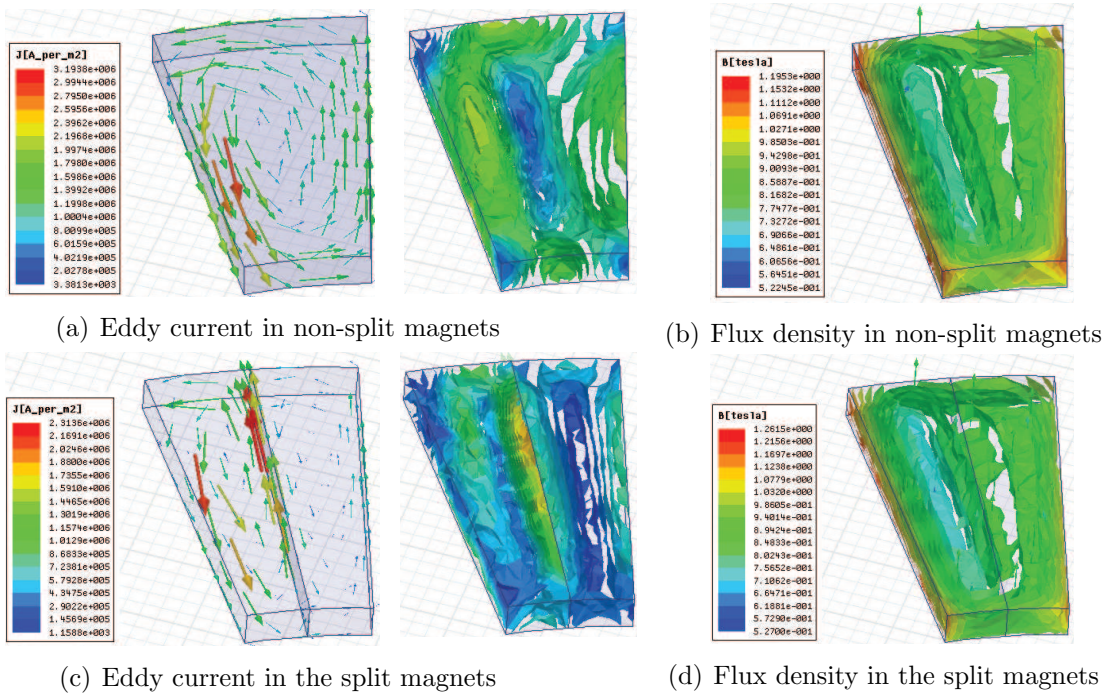


Figure 2.11: Eddy current in non split and split magnets

## 2.5.5 Eddy Current Loss on Various Speeds and Load Conditions

### 2.5.5.1 Eddy Current Loss on Speed Changes

Fig. 2.12 shows the eddy current loss in a solid rotor plate and magnets increases almost linearly with speed.

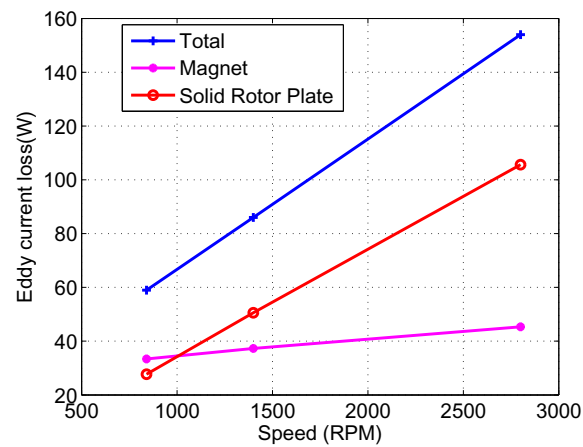


Figure 2.12: Eddy current loss in single layer windings at rated current

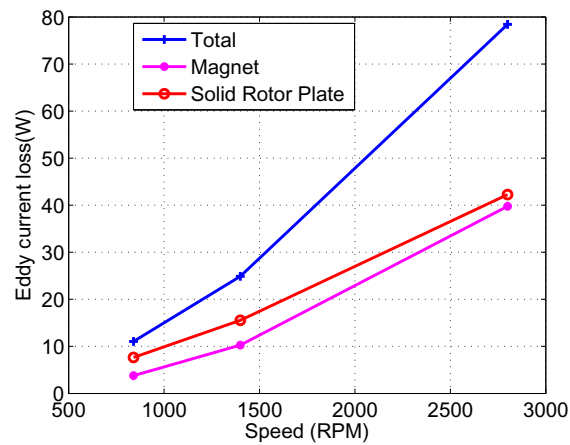


Figure 2.13: Eddy current loss in double layer windings at rated current

### 2.5.5.2 Eddy Current Loss on Current Changes

Fig.2.14 and Fig.2.15 shows that the eddy current loss in the rotor plate increases significantly with current increase in single layer windings than in double layer windings.

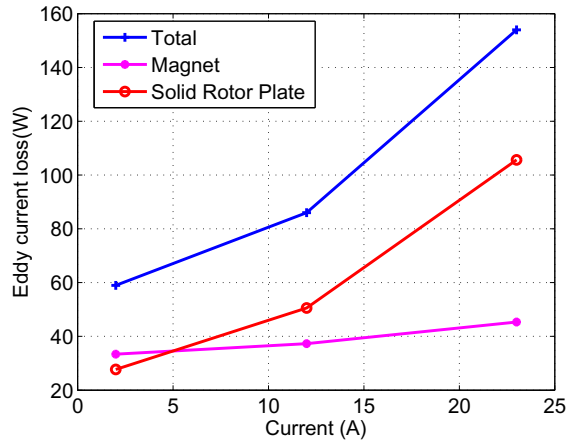


Figure 2.14: Eddy current loss in single layer windings at rated speed

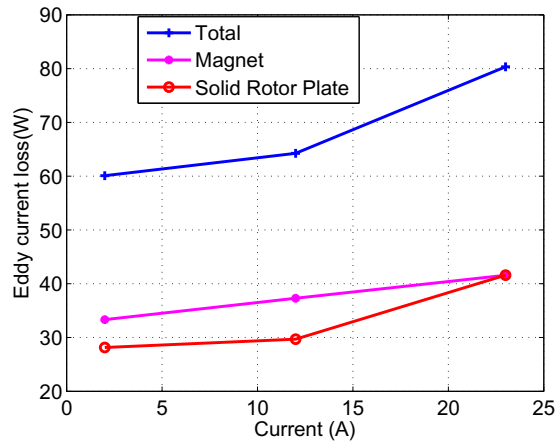


Figure 2.15: Eddy current loss in double layer windings at rated speed

### 2.5.6 Conclusion

As is known, single layer windings have better fault tolerance capability than double layer windings. However from the simulation, it can be seen that there is much more eddy current loss in the solid rotor plate in single layer windings due to the large MMF space harmonics. In double layer winding, stator slotting impacts relatively more on the eddy current loss.

# Chapter 3

## Stator Core Loss Measurement

### 3.1 Introduction

In this chapter, methods are proposed to measure the core loss in a fabricated stator of a single-sided axial flux permanent magnet machine. The core loss data in the back iron and in a single tooth are measured separately, eliminating the use of any correction factor. The core loss data measured in the fabricated stator is compared with measurements made on an identical toroid to the one from which the stator is fabricated by milling slots, before the milling operation. The purpose of this work is to get the actual core loss as accurately as possible for later eddy current loss separation research.

### 3.2 Test Description and Schemes

#### 3.2.1 Description of Test Stator Cores

A single-sided axial flux permanent magnet machine was designed as an integrated starter-alternator for use in a series hybrid vehicle. The specifications for the stator

are: 24 slots, 22 poles, outer radius 98 mm, inner radius 58 mm, slot depth is 35 mm, slot width 8 mm, stator back iron thickness 10 mm. It has single layer non-overlapped windings. The steel grade of the stator is non-grain oriented M12-29G from AK steel.

There are three tests. First, the core loss measurement is carried out on a toroid stator core prior to milling the slots. The second test is to measure the core loss in the back iron of a slotted stator with an excitation current winding around the back iron. The third test is to measure the core loss in a single tooth with an excitation current winding around only one tooth. The details of the tests will be presented below.

### 3.2.2 Test Scheme

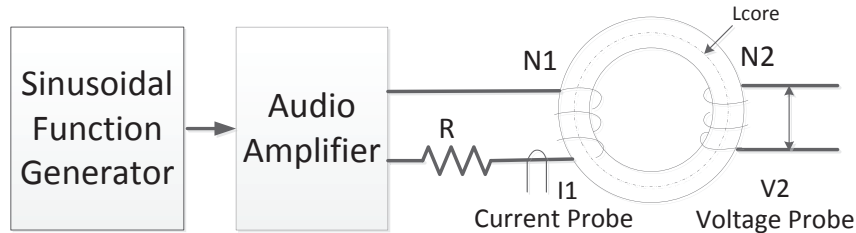


Figure 3.1: Test scheme for core loss measurement

Fig. 3.1 shows the test scheme. Fig. 3.2 shows the test equipment. The function generator, LFG-1300s, provides a sinusoidal voltage at different frequencies and amplitudes. Here the measured frequencies are from 60 Hz to 500 Hz. The audio amplifier, Lanzar MAXP2960N, is used to amplify the sinusoidal voltage from the function generator and provide a current drive. It can provide a maximum power of 600 W (RMS continuously into 4 ohms) when the two channels are bridged. The high power audio amplifier is relatively easy to obtain and costs only a few hundred dollars. A current probe and a differential voltage probe are used to measure the primary exciting current and secondary voltage.

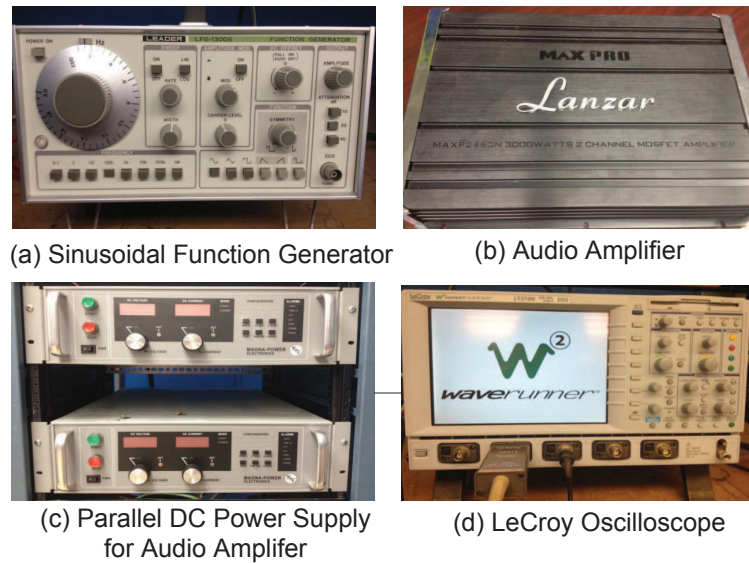


Figure 3.2: Test devices for core loss measurement

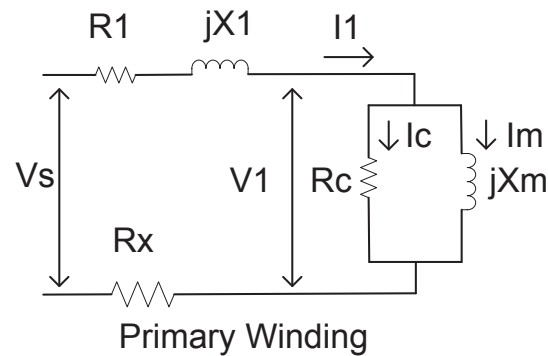


Figure 3.3: Equivalent circuit of the tested toroid

Fig. 3.3 shows the equivalent primary circuit for the tested toroid. In measuring core loss, it is assumed that excitation Voltage  $V_1$  is responsible for core losses modeled  $R_c$ , and with  $I_m$  is the magnetizing current. There is no current in the Geest2012 winding. These are good assumptions since the secondary side voltage probe does not draw any current due to its high impedance [75]. It is also assumed that the flux flowing into the magnetic core is equal to the flux linkage in the primary winding, which means that the flux flowing in the free space around the toroid evaluates to zero. These assumptions can also be checked in 3D FEA.



The magnetic core has two windings. The primary winding is used to create a magnetic field intensity  $H$ , which is:

$$H(t) = \frac{N_1 \cdot I_1(t)}{L_{core}} \quad (3.1)$$

in which  $L_{core}$  is the average magnetic flux path.

The primary winding voltage  $V_1$  is:

$$V_1(t) = N_1 \frac{d\phi(t)}{dt} = N_1 A_{core} \frac{dB(t)}{dt} \quad (3.2)$$

Under pure sinusoidal flux density condition:

$$B(t) = B_m \sin(\omega t) \quad (3.3)$$

Thus,

$$V_1(t) = N_1 A_{core} \omega B_m \cos(\omega t) \quad (3.4)$$

$N_1$  is the number of turns in the primary winding,  $B_m$  is the peak flux density,  $A_{core}$  is the cross sectional area of flux linkage, and  $f$  is the excitation frequency.

The rms voltage of  $V_1(t)$  is:

$$V_1 = \sqrt{2} \pi f N_1 B_m A_{core} \quad (3.5)$$

During the measurement, the number of turns  $N_1$  needs to be manipulated in order not to exceed the voltage limit of the audio amplifier.  $V_1$  is not able to be measured directly, however it could be calculated through the induced voltage in secondary windings.

The induced voltage in the secondary winding is:

$$V_2(t) = N_2 \frac{d\phi(t)}{dt} = N_2 A_{core} \frac{dB(t)}{dt} \quad (3.6)$$

Thus the flux density is:

$$B(t) = \frac{1}{N_2 A_{core}} \int V_2 dt \quad (3.7)$$

$A_{core}$  is the cross section area of flux linkage.

The measured core loss is calculated as:

$$P_{coreloss} = \frac{1}{T} \frac{N_1}{N_2} \int_0^T V_2 \cdot I_1 dt \quad (3.8)$$

T is the period of the waveform. If written in sampled data is:

$$P_{coreloss} = \frac{N_1}{N_2} \frac{1}{K} \sum_{k=1}^K V_2[k] \cdot I_1[k] \quad (3.9)$$

K is the number of samples in one period,  $N_1$  is the number of turns in the primary windings,  $N_2$  is the number of turns in the secondary windings.

The core loss per unit mass (watt/lbs) will be:

$$p_{coreloss} = \frac{P_{coreloss}}{\rho \cdot h \pi (R_o^2 - R_i^2)} \quad (3.10)$$

$\rho$  is the mass density of the steel,  $h$  is the height of the toroid,  $R_o$ ,  $R_i$  is the outer and inner radius. The detailed calculations can be found in [76].

From the(3.1)(3.7)(3.8), it could also found that the core loss equals to the area of

BH loop per cycle multiplied by frequency.

$$P_{coreloss} = \frac{1}{T} \int_0^T B(t)H(t)dt \cdot A_{core}L_{core} \quad (3.11)$$

in which  $A_{core}L_{core}$  is the volume of the test toroid.

### 3.3 Core Loss Measurement in Unslotted Toroid

#### 3.3.1 Test Verification at 60 Hz Compared with Steel Manufacturer's Data

The test system is set up according to 2.2.2. The unslotted toroid stator is shown in Fig. 3.4. In order to validate the accuracy of the system, the core loss measurement at 60 Hz is performed and compared with the only available data from the steel manufacture. From Fig. 3.5 and Fig. 3.6, it shows good agreement between the measured data and the original data from AK steel.



Figure 3.4: Unslotted toroid for core loss measurement

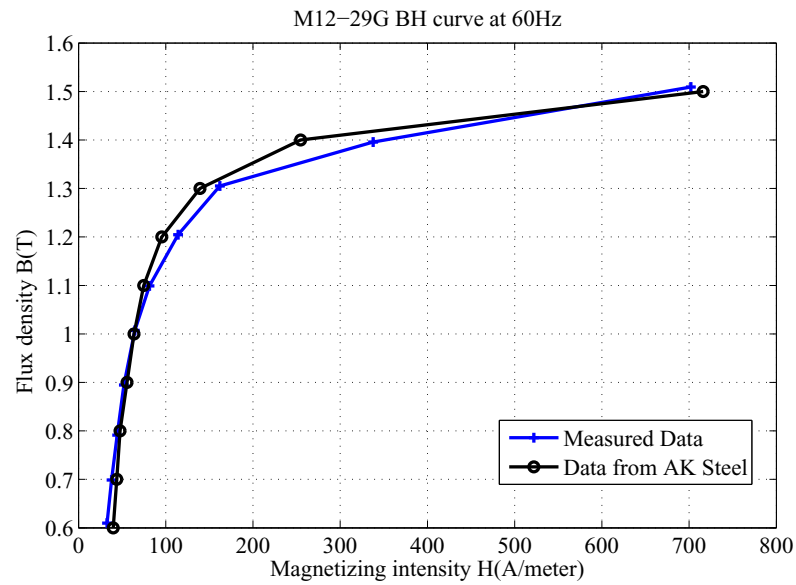


Figure 3.5: M12-29G BH curves in unslotted toroid at 60 Hz

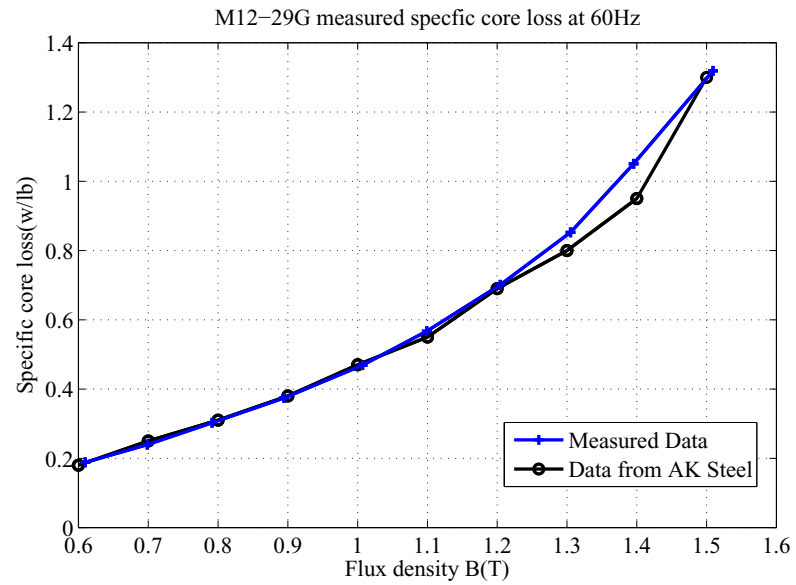
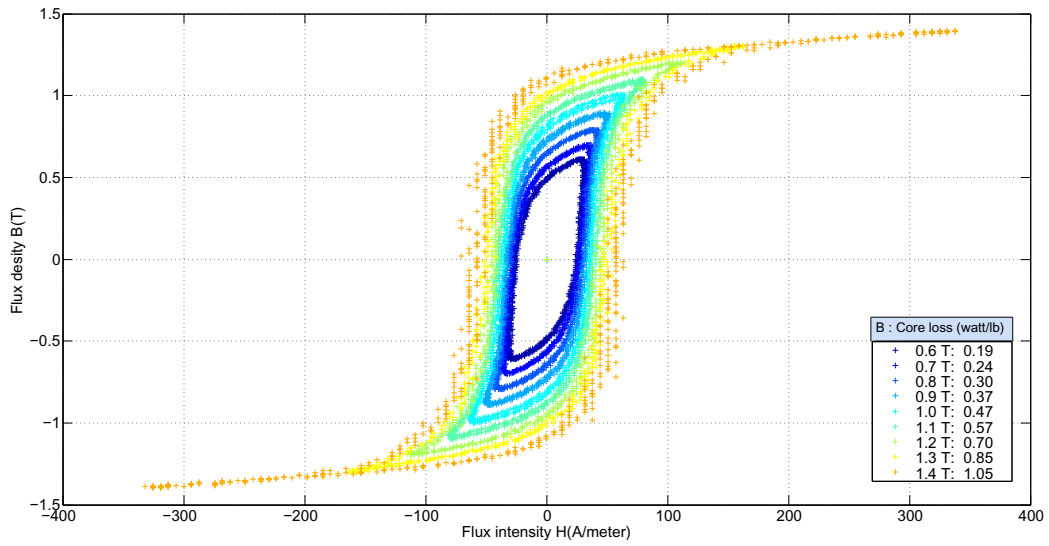


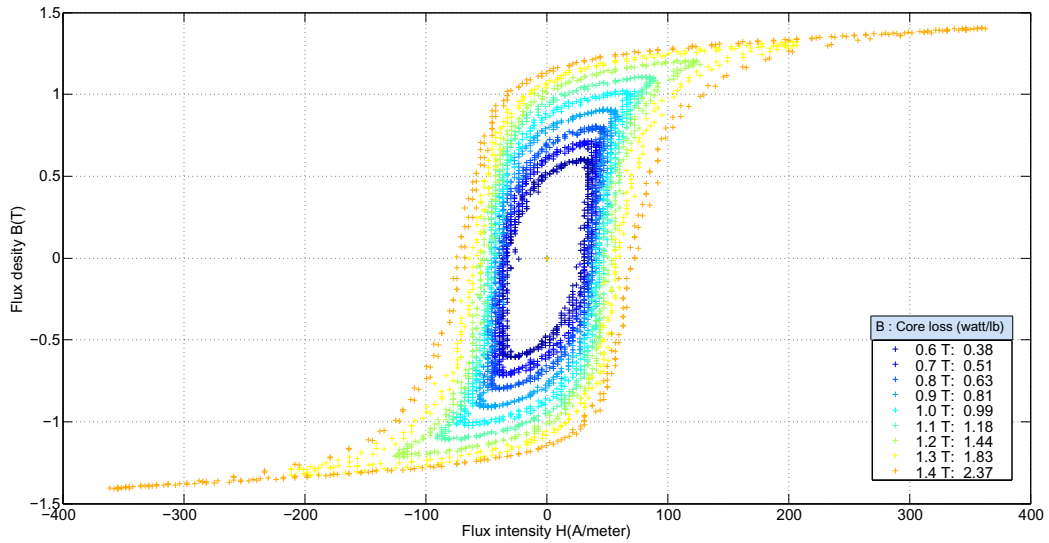
Figure 3.6: M12-29G measured specific core loss in unslotted toroid at 60 Hz

### 3.3.2 Results at Frequencies (60 Hz, 100 Hz, 200 Hz, 300 Hz, 400 Hz, 500 Hz)

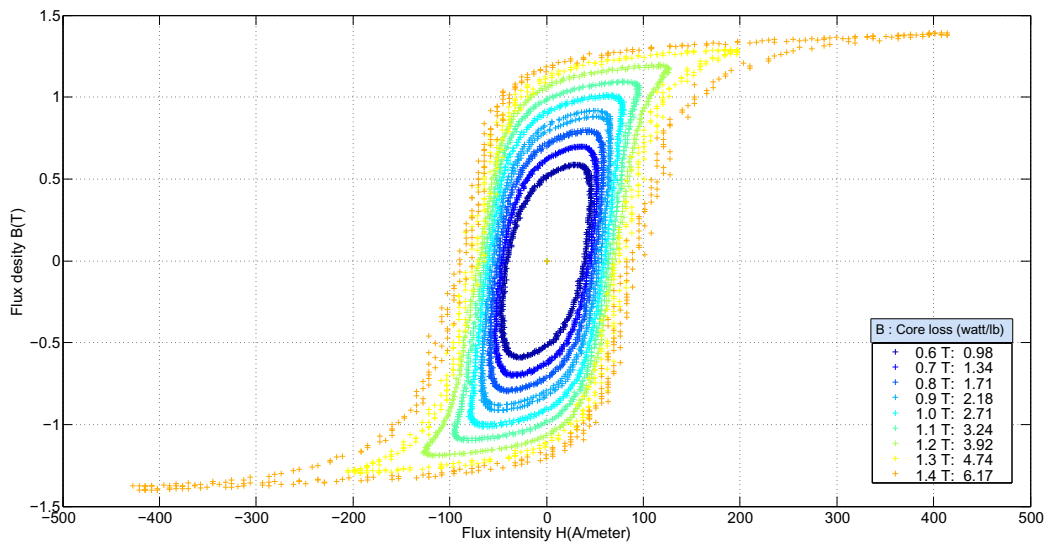
Fig. 3.7. and Fig. 3.8 shows the plotted B-H loops. Fig. 3.9 shows the average core loss at peak flux levels from 0.6 T to 1.4 T at different frequencies.



(a) 60 Hz

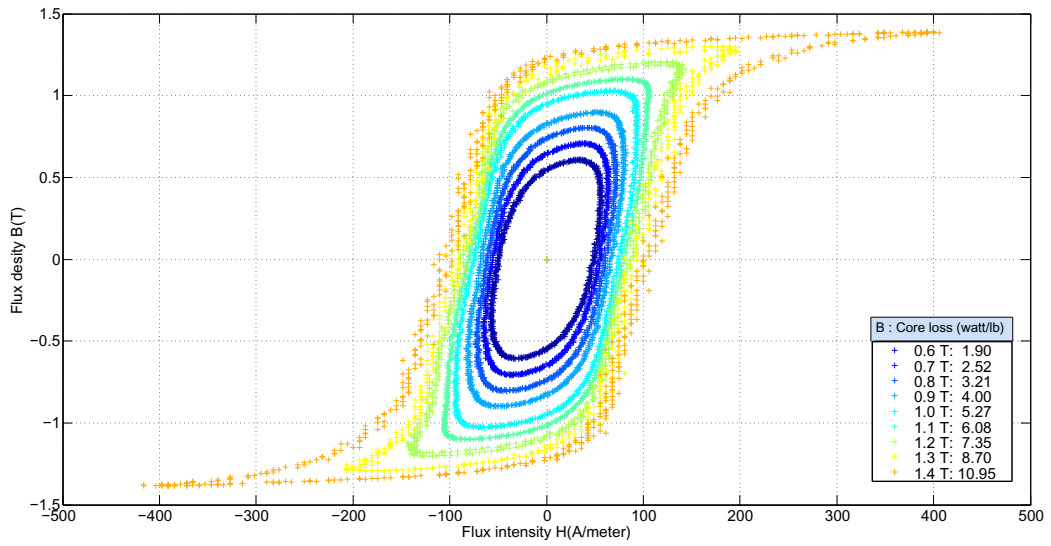


(b) 100 Hz

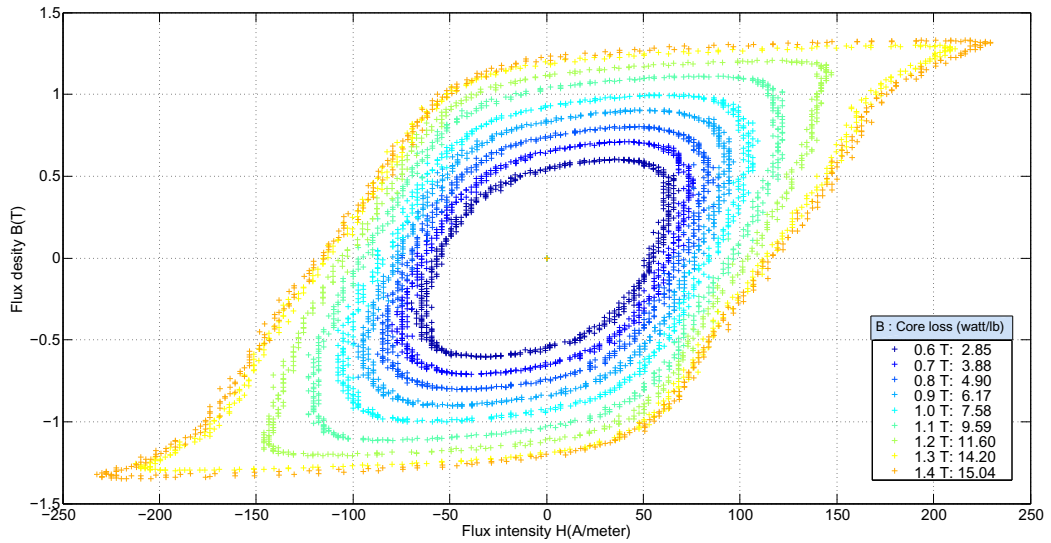


(c) 200 Hz

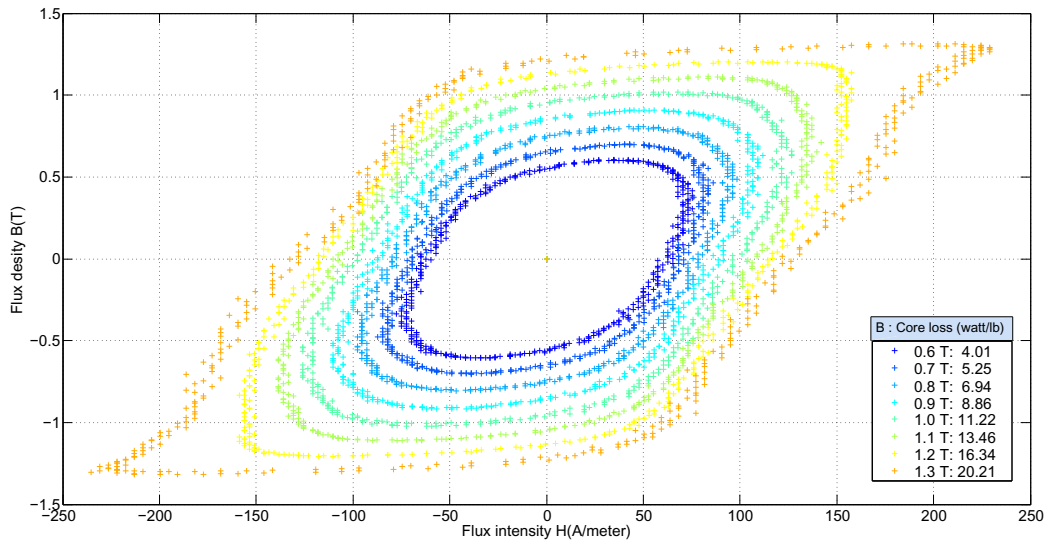
Figure 3.7: M12-29G BH loops at 60 Hz, 100 Hz, 200 Hz



(a) 300 Hz



(b) 400 Hz



(c) 500 Hz

Figure 3.8: M12-29G BH loops at 300 Hz, 400 Hz, 500 Hz

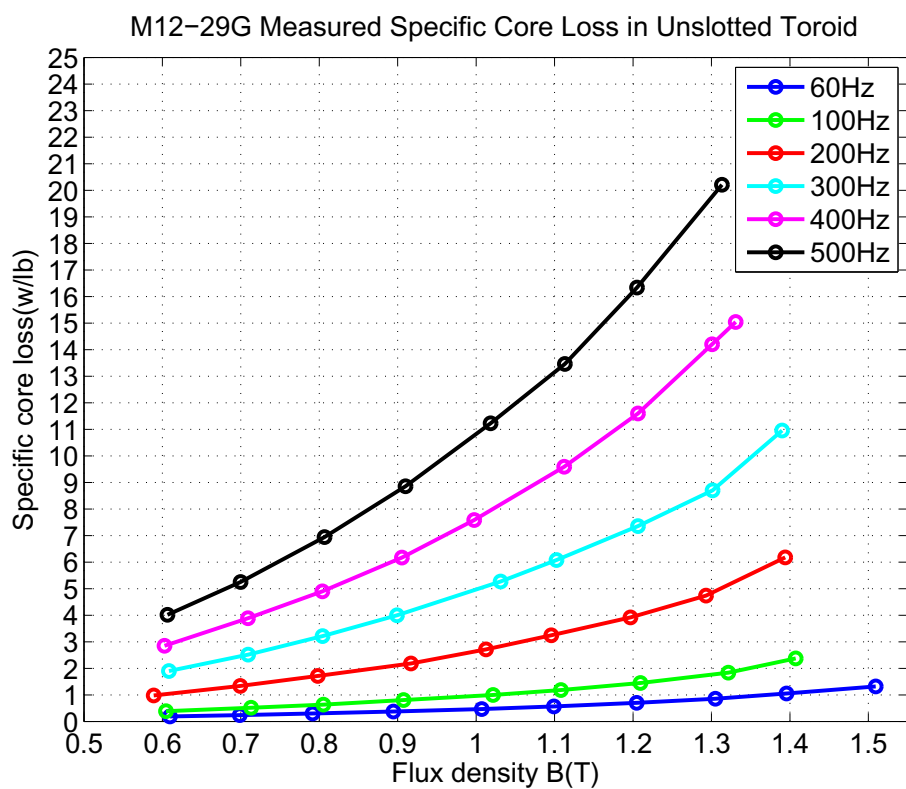
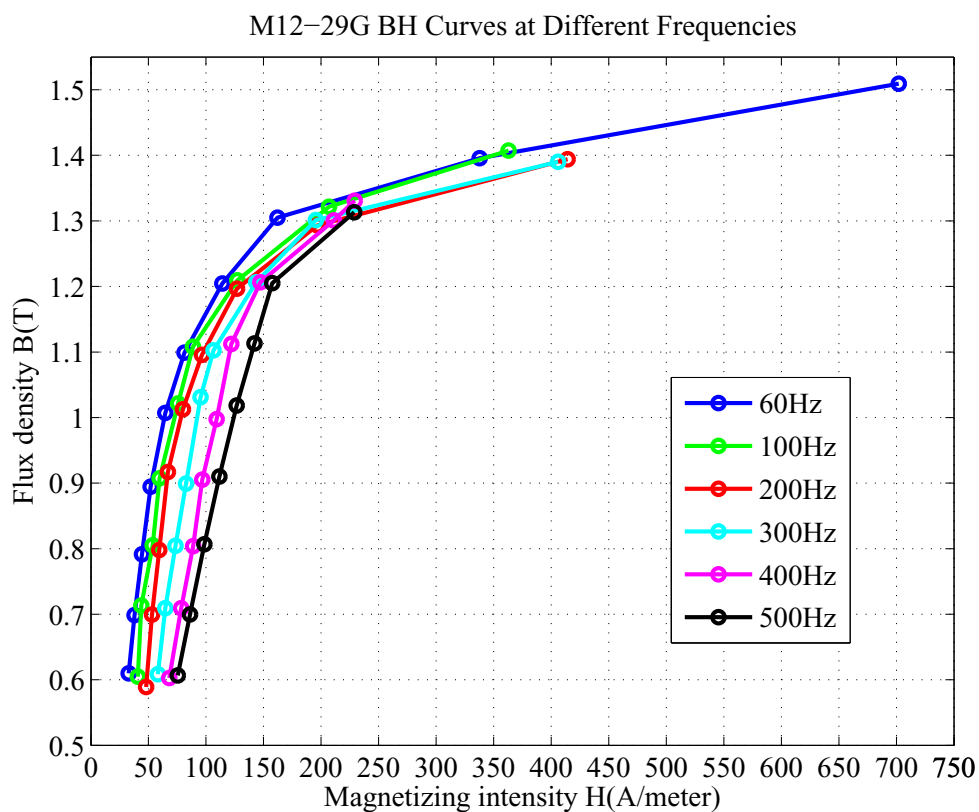


Figure 3.9: Experiment results for core loss measurement in unslotted toroid

## 3.4 Core Loss Measurement in Back Iron

Measurements on the fabricated core will attempt to estimate separately the core loss in the teeth and in the back iron. The flux linkage direction in back iron is parallel to the rolling direction of steel, however the flux linkage direction in the teeth is across the rolling direction. Although the electrical steel used M12-29G is classified as non-grain oriented steel, anisotropy might still exist. Moreover, the milled edges in the tooth could increase the core loss.

### 3.4.1 FEA Simulations

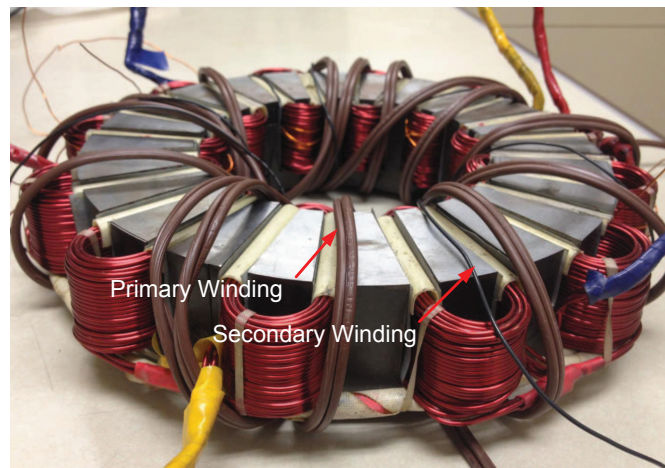


Figure 3.10: Core loss measurement in back iron

A 3D FEA model is set up as shown in Fig. 3.11 according to Fig. 3.10. The excitation current in the primary winding sets up the flux linkage in the magnetic core. In the FEA model, the secondary winding is ignored. This test is similar to the test of the unslotted toroid. However, the flux linkage shown in Fig. 3.12 indicates that there is flux flowing up into the tooth as it passes under a tooth. Thus in the experiment shown in Fig. 3.10, the measured core loss will include the loss in



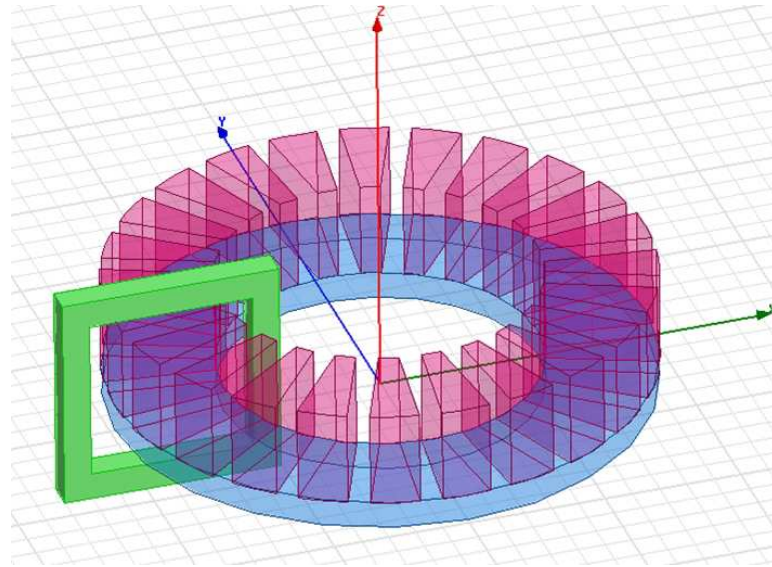
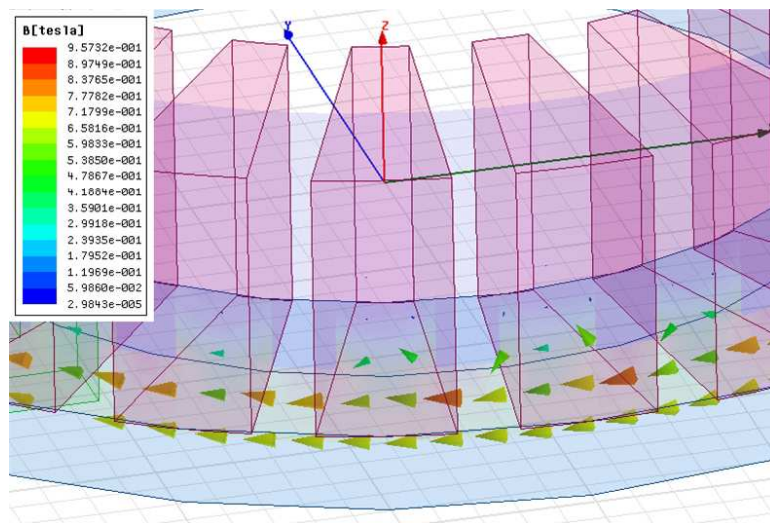


Figure 3.11: FEA model for core loss measurement in back iron

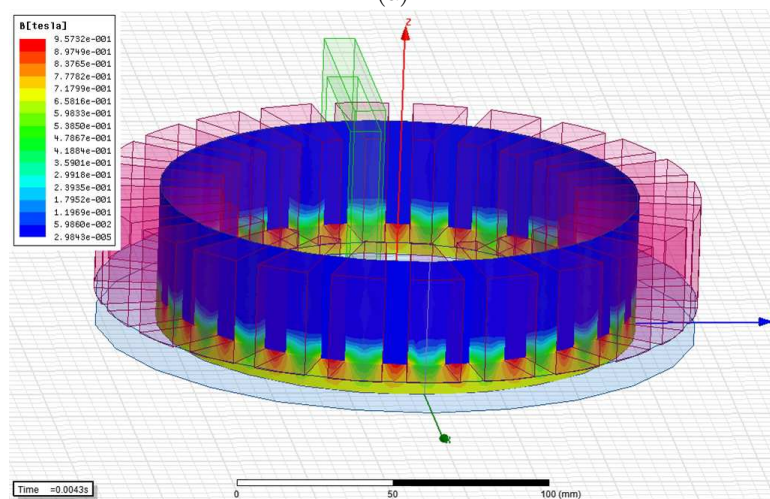
the teeth, which needs to be computed and subtracted. The core losses in different volumes can be calculated separately in the FEA. The FEA results are shown at a 60 Hz sinusoidal current excitation in Fig. 3.12 (c). The red line is the total core loss, the blue line is the core loss in back iron, and the green line is the core loss in the teeth. The loss in back iron accounts for 92% of the total loss. The purpose of the FEA is not to attempt to establish the actual level of core loss, but to establish a “split ratio” to apply to the single measured loss number, to isolate the losses in the back iron alone. This number does not change with frequencies and flux densities in FEA simulation results.

### 3.4.2 Experimental Results

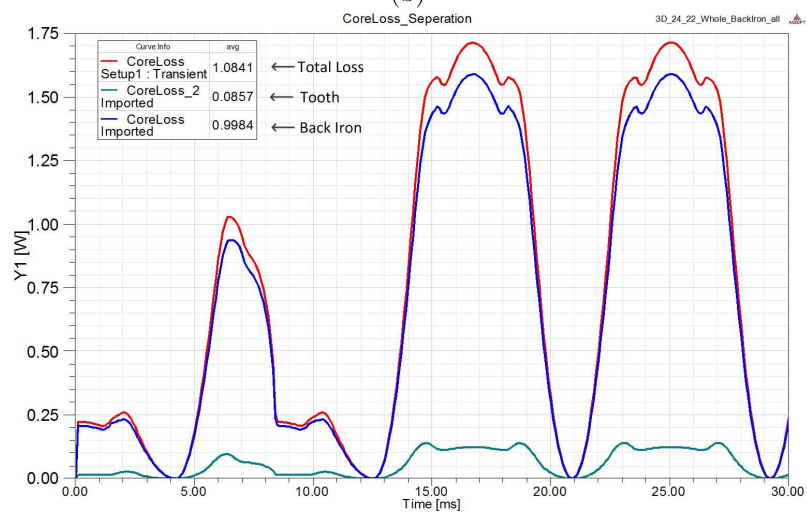
The measured current  $I_1$  and voltage  $V_2$  is shown in Fig. 3.13(a) as an example. The result of core loss measurements in the back iron at various flux densities is shown in Fig. 3.13(b). The detailed data are shown in Table. I. It can be seen that the back iron loss is close to the core loss measured in the unslotted toroid.



(a)

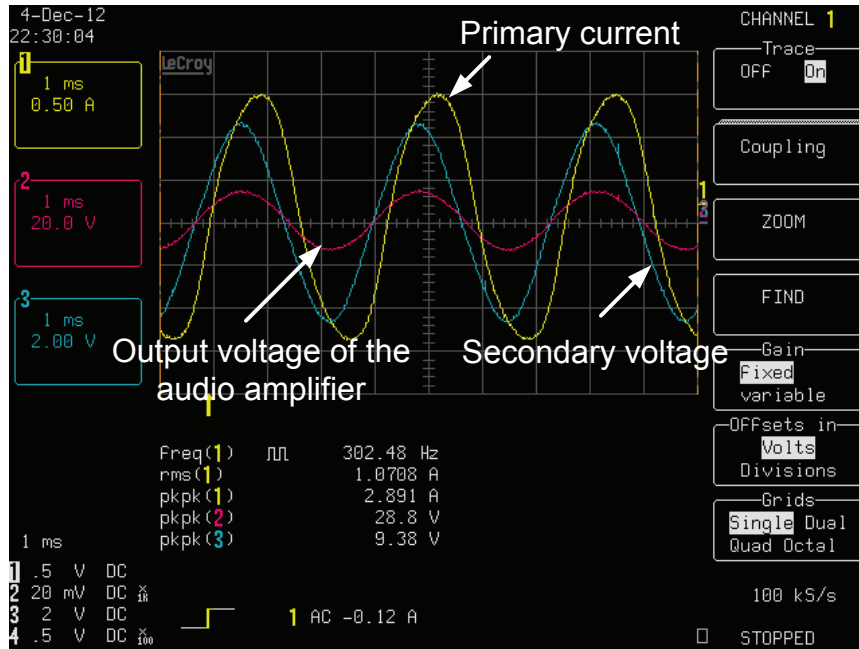


(b)

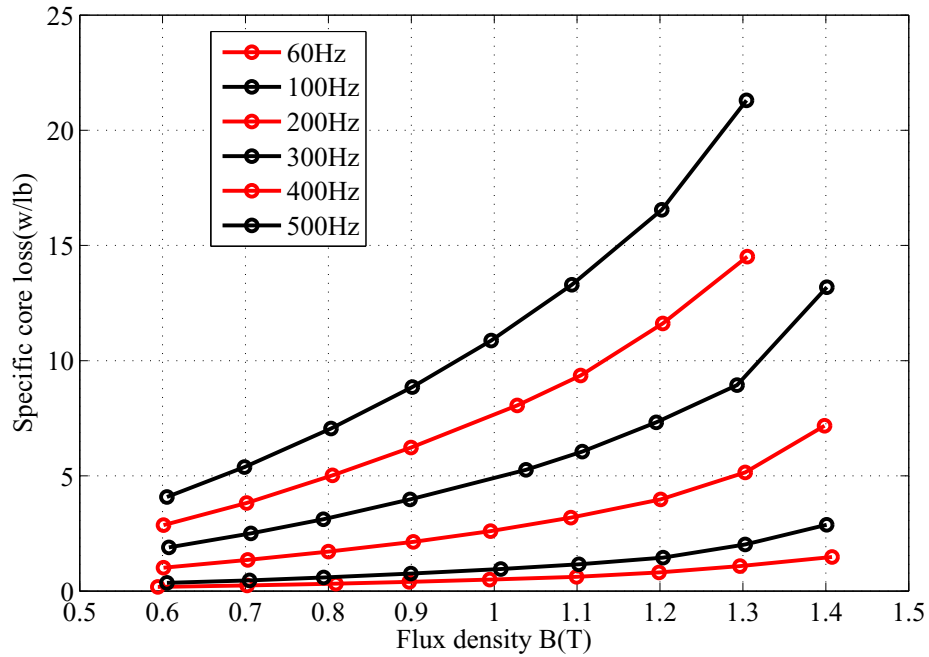


(c)

Figure 3.12: FEA results for core loss measurement in back iron



(a) Primary current I1 and secondary voltage V2 at 300 Hz, 0.6 T



(b) Specific core loss data in back iron with 92% split ratio

Figure 3.13: Experiment results for core loss measurement in back iron

## 3.5 Core Loss Measurement in the Teeth

The specific core loss in the teeth could be measured under three conditions, when only one tooth is excited, when all the coils of one phase (four teeth) are excited and when all three phases (twelve teeth) are excited by the same sinusoidal current. The purpose of three tests is to ensure that the core loss measurement is as accurate as possible. FEA simulations are implemented first. The purpose of FEA simulation is to obtain the “split ratio” to separate the loss in teeth only from the measured loss in the experiments. In the experiment, the measured loss is a total loss, includes the loss in the uncut toroid, the loss in other unexcited teeth and the loss in stator back iron. The winding resistance loss is so small as to be negligible.

### 3.5.1 Method 1: Core Loss Measured at One Tooth Excited

#### 3.5.1.1 FEA Simulations

A 3D FEA model is set up as shown in Fig. 3.14. The unslotted toroid is put on the top of the finished stator to close the flux linkage path. The mating surfaces are ground to provide the minimum possible air gap. However, there will be still be tiny air gaps which should be taken care of in the FEA simulations.

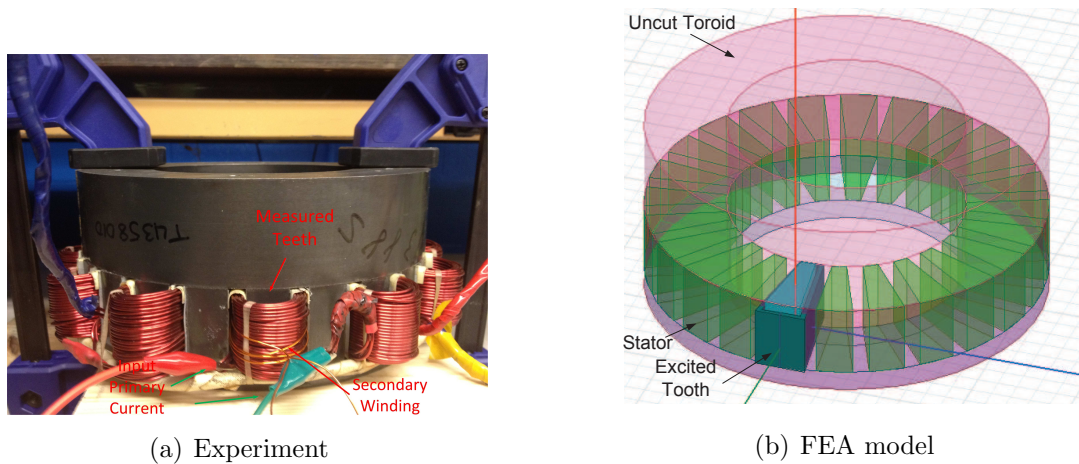


Figure 3.14: Core loss measurement at one tooth excited

The steps to obtain the split ratio are:

(1) In the experiment, choose a frequency, with a certain current, and calculate the flux density in the tooth from secondary voltage.

(2) In the 3-D FEA model, excite the same current in the single tooth and adjust the air gap to get the same flux density.

(3) In the 3-D FEA model, compute the loss in tooth only and the total loss. Thus the split ratio would be obtained. Here is an example of when current value is 2.672 A and the flux density is 0.6 T as in Fig. 3.15.

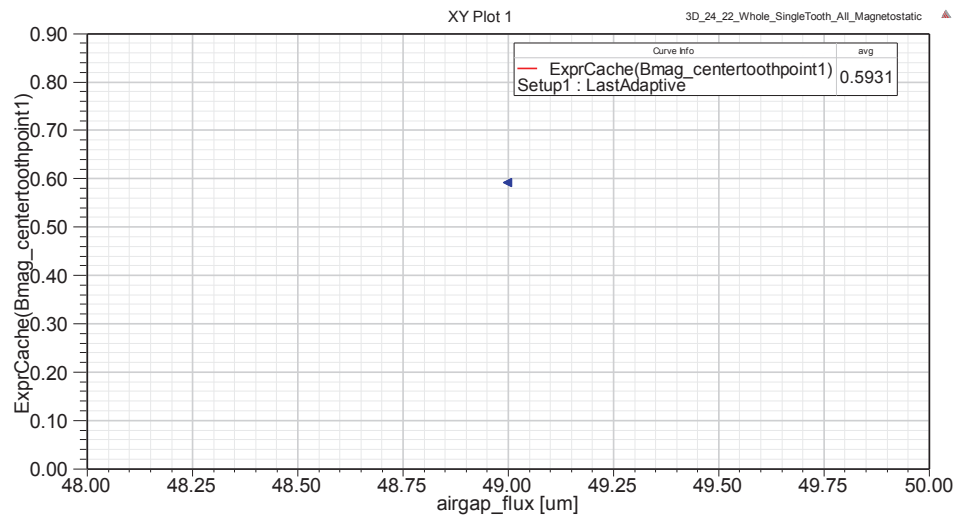
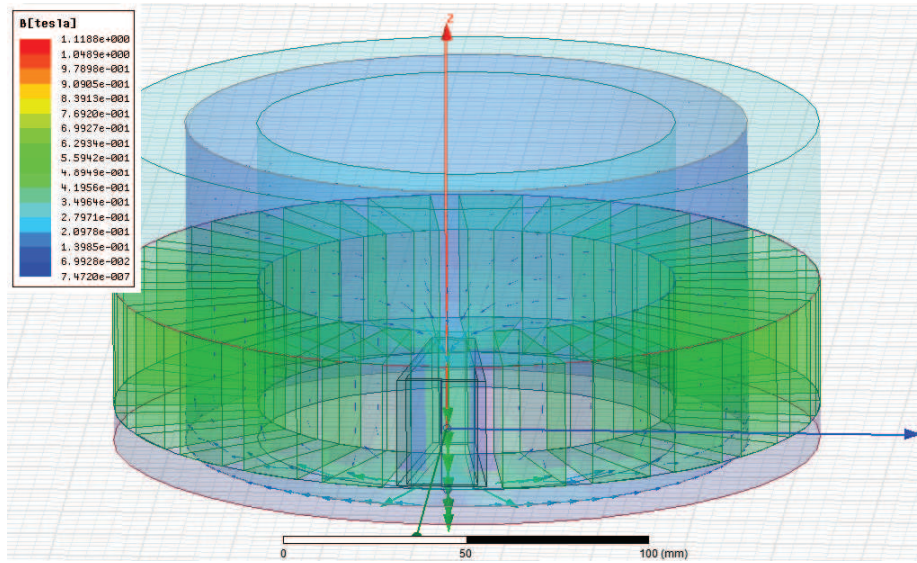
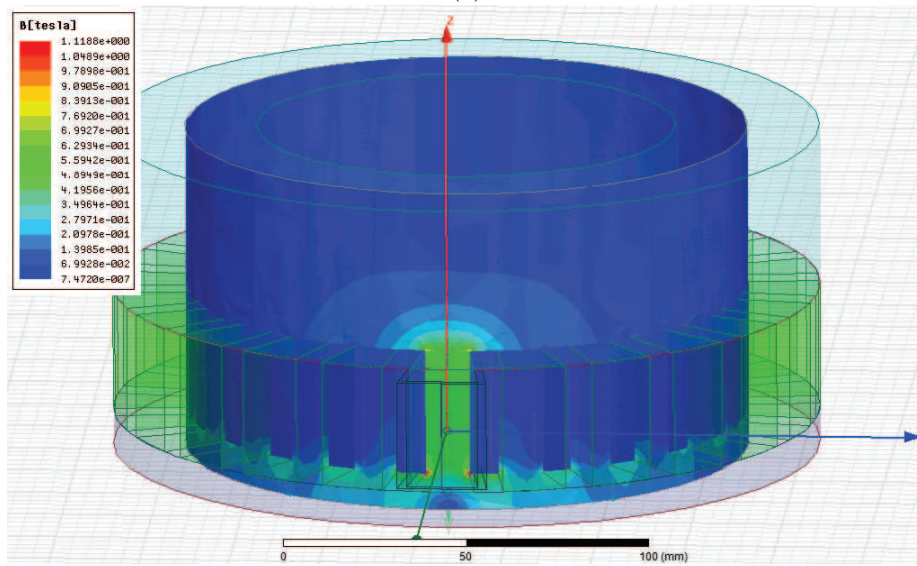


Figure 3.15: Air gap adjustment

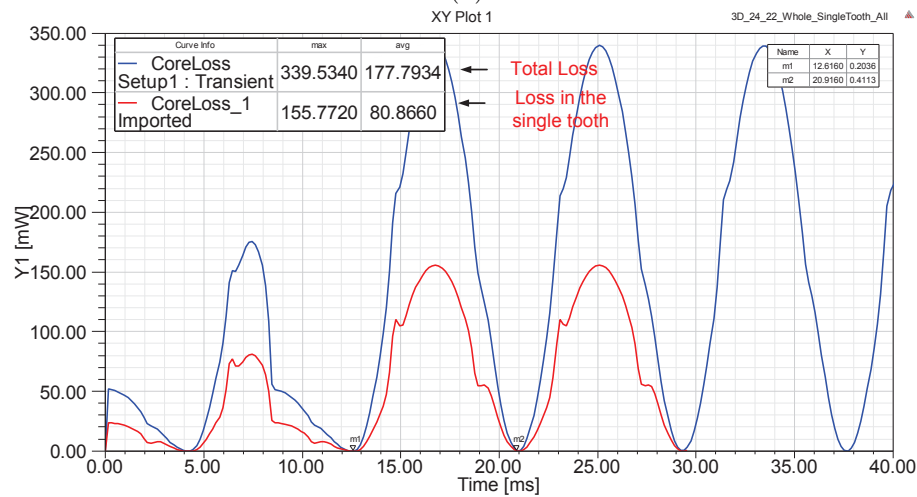
The FEA core loss separation results are shown in Fig. 3.16. It can be seen that the single tooth loss accounts for 45% of the total loss measured at 60 Hz sinusoidal excitation current. It has been determined through testing that this split ratio does not change much with frequencies and flux densities in FEA simulation results. It varies slightly from 44.7% to 45.2%. Thus the split ratio is set at 45%.



(a)



(b)



(c)

Figure 3.16: FEA results for core loss measurement at one tooth excited

### 3.5.1.2 Experimental Results

The experiment's results, manipulated to represent the core loss, of a single tooth at different frequencies and various flux densities are shown in Fig.3.17. The exact measured loss data with a 45% split is shown in Table.I. It can be seen that the core loss in the single tooth is in the range of 1.5-2.1 higher than that in measured unslotted toroid or back iron.

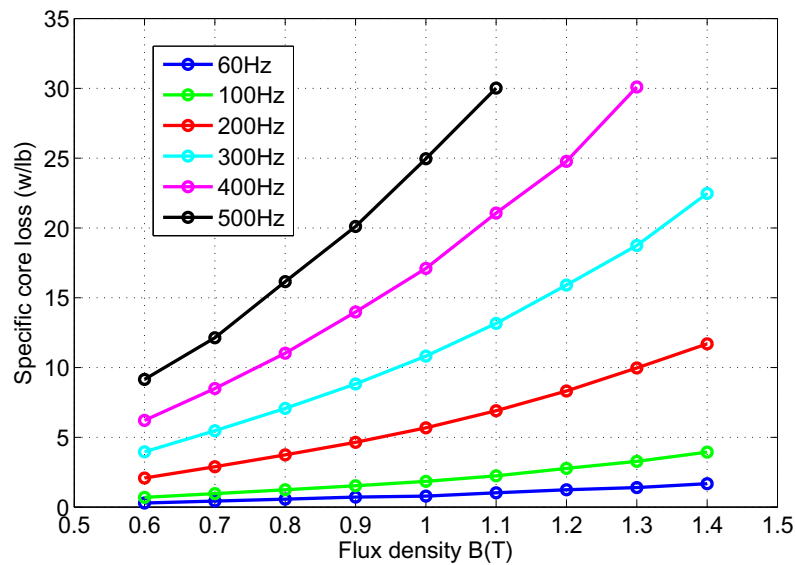


Figure 3.17: Experiment results for core loss measurement at one tooth excited

### 3.5.2 Method 2: Core Loss Measured at One Phase (Four) Teeth Excited

Method 2 consists of an approach similar to that used in Method 1. In the fabricated single layer winding stator, the primary current is excited into a winding of one phase. Four teeth are excited. In the FEA simulation, the split ratio is obtained similarly in order to separate the loss in the excited four teeth from the total measured loss. It is expected that this would be more accurate since the loss data in one tooth is the average value of the loss in four teeth.

### 3.5.2.1 FEA Simulations

As shown in Fig.3.18, the split ratio is 31 %.

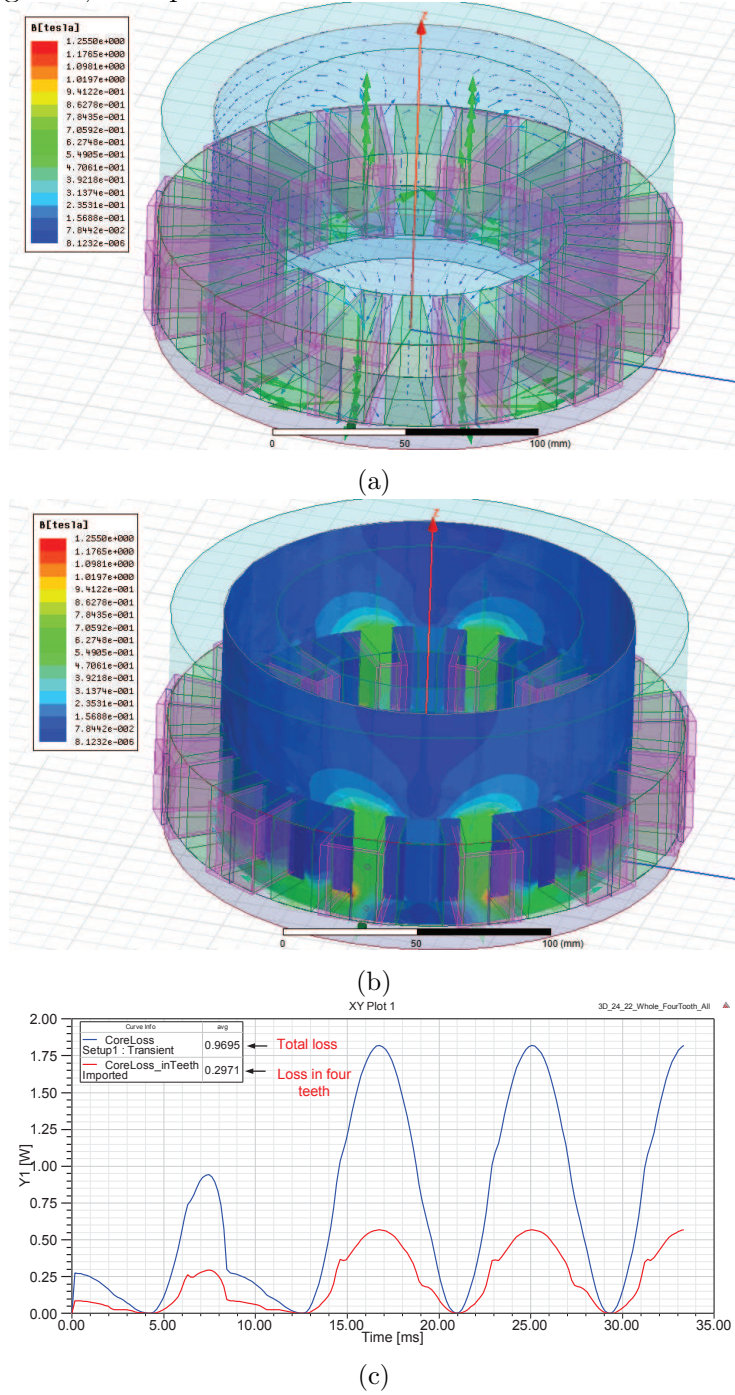


Figure 3.18: FEA results for core loss measurement at one phase (four) teeth excited



### 3.5.2.2 Experimental Results

The secondary voltages measured at the excited teeth are shown as in Fig. 3.21. It shows that these two voltages are close, which means they are experiencing the same core loss. The measured specific core loss manipulated with 31% split ratio is shown in Fig. 3.20. As to the voltage and current limitation of the audio amplifier, high frequency data cannot be reached.

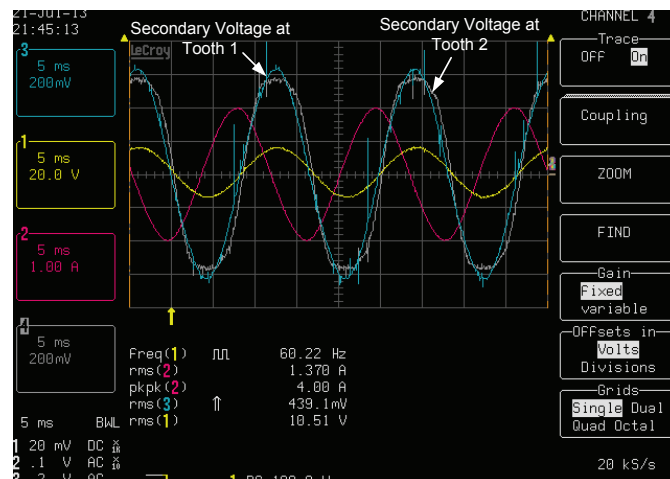


Figure 3.19: Secondary voltages of different teeth at one phase (four) teeth excited

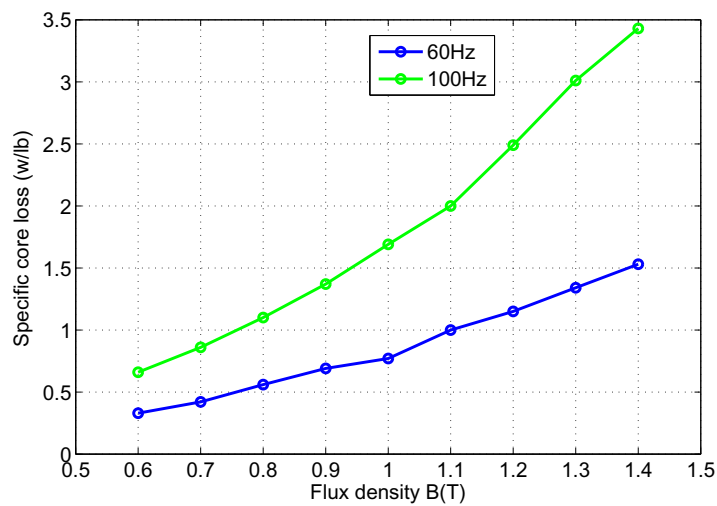


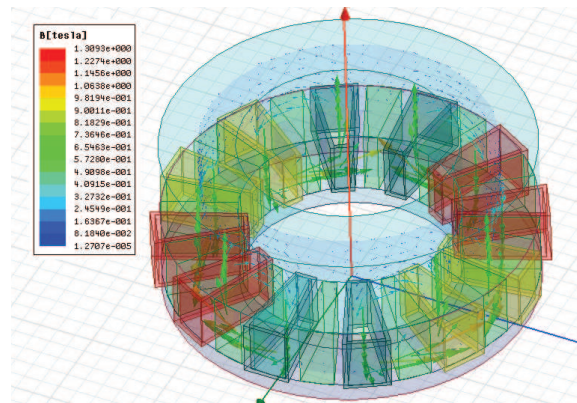
Figure 3.20: Experiment results for core loss measurement at one phase (four) teeth excited

### 3.5.3 Method 3: Core Loss Measured at Three Phases

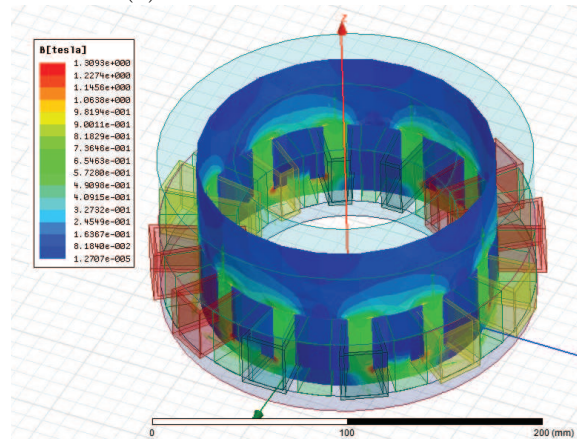
#### (Twelve) Teeth Excited

##### 3.5.3.1 FEA Simulations

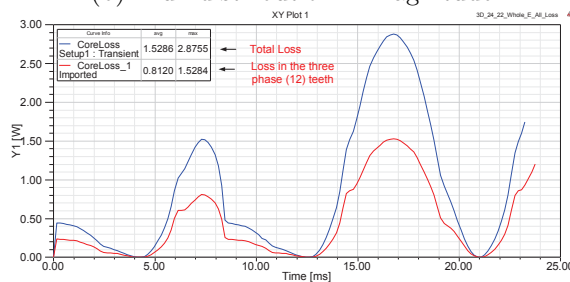
The split ratio is 53 %.



(a) Flux distribution B vector



(b) Flux distribution B magnitude

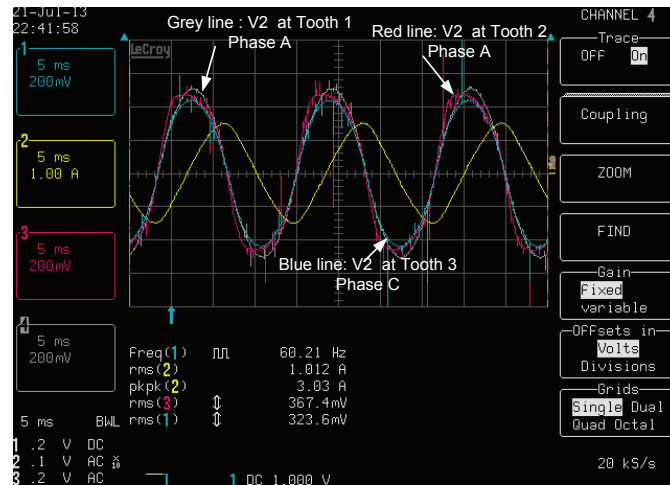


(c) Loss in three phases (twelve) excited FEA model

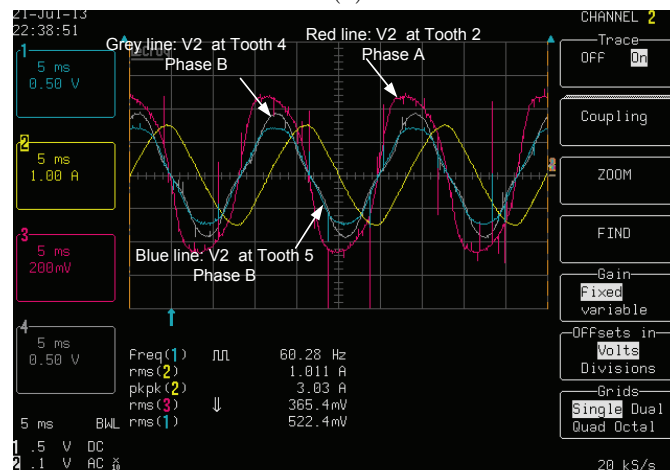
Figure 3.21: FEA model at three phases (twelve) teeth excited

### 3.5.3.2 Experimental Results

In this experiment, twelve teeth are excited. Here the secondary voltage measured at five teeth is shown in Fig.3.22.



(a)



(b)

Figure 3.22: Secondary voltages of different teeth at three phases (twelve) teeth excited

It seems that secondary voltages at some teeth are pretty close in phases A and phase C, while the other two teeth at phase B are different. Thus the loss in teeth is not exactly even in each tooth. Thus when measuring the core loss in each tooth, it is necessary to average them. The more the teeth are excited, the more accurate the

results.

Due to the voltage and current limitation of the audio amplifier, only a few data at 60 Hz can be reached.

### 3.5.4 Comparison of Teeth Loss Results by the Three Methods

The measured specific core loss data at 60 Hz by these three methods are compared. They are close which shows the correctness of the methods proposed. In Method 3, when 12 teeth are excited, it should give the most accurate value, the measured loss is lower than when Method 1 and Method 2. However due to limitations, high frequencies can not be reached.

Table 3.1: Comparison of Measured Specific Core Loss Data at 60 Hz By Three Methods

| Flux Density (B)  | 0.6T | 0.7T | 0.8T | 0.9T | 1.0T | 1.1T | 1.2T | 1.3T | 1.4T |
|-------------------|------|------|------|------|------|------|------|------|------|
| One Tooth Excited | 0.29 | 0.43 | 0.57 | 0.72 | 0.79 | 1.02 | 1.24 | 1.40 | 1.67 |
| 4 Teeth Excited   | 0.33 | 0.42 | 0.56 | 0.69 | 0.77 | 1.00 | 1.15 | 1.34 | 1.53 |
| 12 Teeth Excited  | 0.31 | 0.40 | 0.55 | N/A  | N/A  | N/A  | N/A  | N/A  | N/A  |

It is also shown that the specific core loss in the teeth is in the range of 1.5-1.7 times higher than that measured in the back iron.

## 3.6 Conclusion

In this chapter, methods are proposed to measure the core loss in the back iron and in the teeth of a fabricated stator of a single-sided AFPM. FEA simulations are implemented, together with the measured total loss, to obtain the specific core loss

data in the back iron only and in the teeth only. It is shown that during the three methods of measuring the specific core loss in teeth only, the most accurate results can be obtained when three phase teeth are excited. However due to equipment limitations, core loss data at higher frequencies cannot be reached.

Table 3.2: Manipulated Measured Loss Data of M12-29G

| M12-29G Iron loss (watt/lb) |   |      |        |       |       |       |        |       |       |
|-----------------------------|---|------|--------|-------|-------|-------|--------|-------|-------|
| 60 Hz                       |   |      | 100 Hz |       |       |       | 200 Hz |       |       |
| B(T)                        | from left to right are losses in: Unslotted Toroid, Back Iron and Teeth |      |        |       |       |       |        |       |       |
| 0.6                         | 0.19  | 0.18 | 0.29   | 0.38  | 0.36  | 0.70  | 0.98   | 1.01  | 20.8  |
| 0.7                         | 0.24  | 0.24 | 0.43   | 0.51  | 0.46  | 0.96  | 1.34   | 1.35  | 2.89  |
| 0.8                         | 0.30  | 0.32 | 0.57   | 0.63  | 0.59  | 1.24  | 1.71   | 1.71  | 3.74  |
| 0.9                         | 0.37  | 0.40 | 0.72   | 0.81  | 0.76  | 1.53  | 2.18   | 2.13  | 4.64  |
| 1.0                         | 0.47  | 0.49 | 0.79   | 0.99  | 0.96  | 1.84  | 2.71   | 2.60  | 5.68  |
| 1.1                         | 0.57  | 0.62 | 1.02   | 1.18  | 1.16  | 2.24  | 3.24   | 3.19  | 6.90  |
| 1.2                         | 0.70  | 0.81 | 1.24   | 1.44  | 1.45  | 2.77  | 3.92   | 3.98  | 8.32  |
| 1.3                         | 0.85  | 1.08 | 1.40   | 1.83  | 2.02  | 3.28  | 4.74   | 5.15  | 9.97  |
| 300 Hz                      |   |      | 400 Hz |       |       |       | 500 Hz |       |       |
| 0.6                         | 1.90  | 1.90 | 3.96   | 2.85  | 2.87  | 6.21  | 4.01   | 4.08  | 9.15  |
| 0.7                         | 2.52  | 2.50 | 5.47   | 3.88  | 3.83  | 8.49  | 5.25   | 5.38  | 12.13 |
| 0.8                         | 3.21  | 3.11 | 7.07   | 4.90  | 5.03  | 11.02 | 6.94   | 7.05  | 16.15 |
| 0.9                         | 4.00  | 3.98 | 8.82   | 6.17  | 6.23  | 13.98 | 8.86   | 8.86  | 20.10 |
| 1.0                         | 5.27  | 5.26 | 10.82  | 7.58  | 8.06  | 17.10 | 11.22  | 10.87 | 24.96 |
| 1.1                         | 6.08  | 6.05 | 13.16  | 9.59  | 9.36  | 21.06 | 13.46  | 13.29 | 30.01 |
| 1.2                         | 7.35  | 7.32 | 15.90  | 11.60 | 11.61 | 24.77 | 16.34  | 16.55 | N/A   |
| 1.3                         | 8.70  | 8.93 | 18.74  | 14.20 | 14.51 | 30.09 | 20.21  | 21.30 | N/A   |

\*Loss data in the teeth is collected at one tooth excited.

# Chapter 4

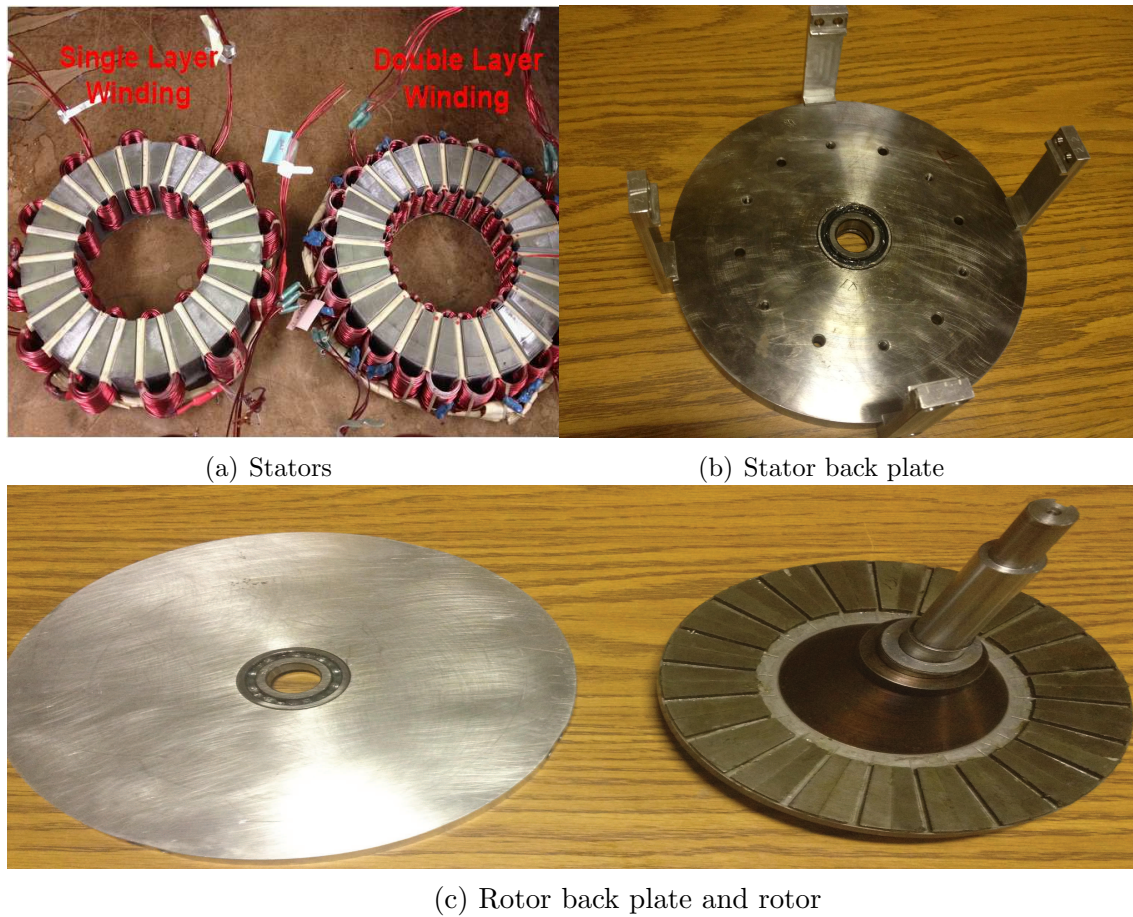
## Experiment Verification

### 4.1 Introduction

In this chapter, the two single-sided AFPM machines are assembled. Machine parameters are tested to ensure a match to original design. The machines are tested at no load and loaded conditions. Methods of segregation are illustrated. Eddy current loss in the rotor and magnets is separated and compared with FEA simulations.

### 4.2 Assembling of the Single-Sided AFPMs

The parts of the single-sided AFPMs tested include the stators of single layer winding and double layer winding, stator back plate, rotor and rotor back plate are shown in Figure 4.1. There are two concerns when assembling them together: the axial attractive force and air gap maintenance. The attractive magnetic force between the stator and rotor imposes a high axial load, which needs to be considered in the bearing selection. Improper selection will cause bearing failures. Through FEA simulations when the airgap is 1mm, the axial force is about 2840 Newton. A single row angular



(a) Stators

(b) Stator back plate

(c) Rotor back plate and rotor

Figure 4.1: Parts of the single-sided AFPM Machines

contact bearing SKF 7205, which in the stator back plate, is selected to take the axial load and a Koyo 6205 single row deep groove ball bearing, which is in the rotor back plate, is chosen to stabilize and position the rotor and shaft to maintain an equal airgap all the way around the stator and prevent wobbling. The bearings are unsealed and greased to eliminate friction loss. Shims are used to maintain the air gap. Equipment is designed to introduce the rotor plate to the stator gradually.

A drawing of the assembled machines is shown in Figure 4.2. The two assembled machines are shown in Figure 4.3.

It should be noted that there is a slightly difference in the air gap in these two machines. The average air gap in the single layer one is about 1.68 mm while the

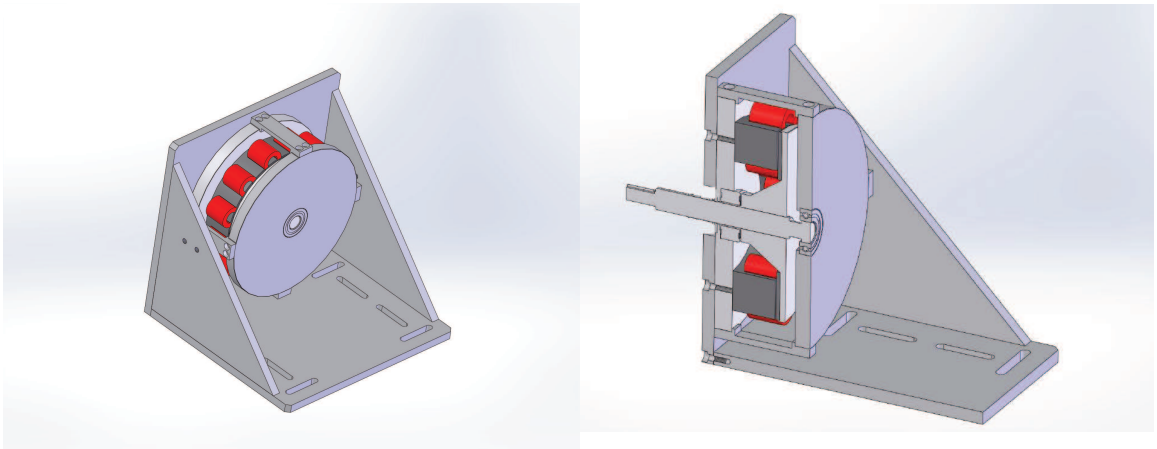
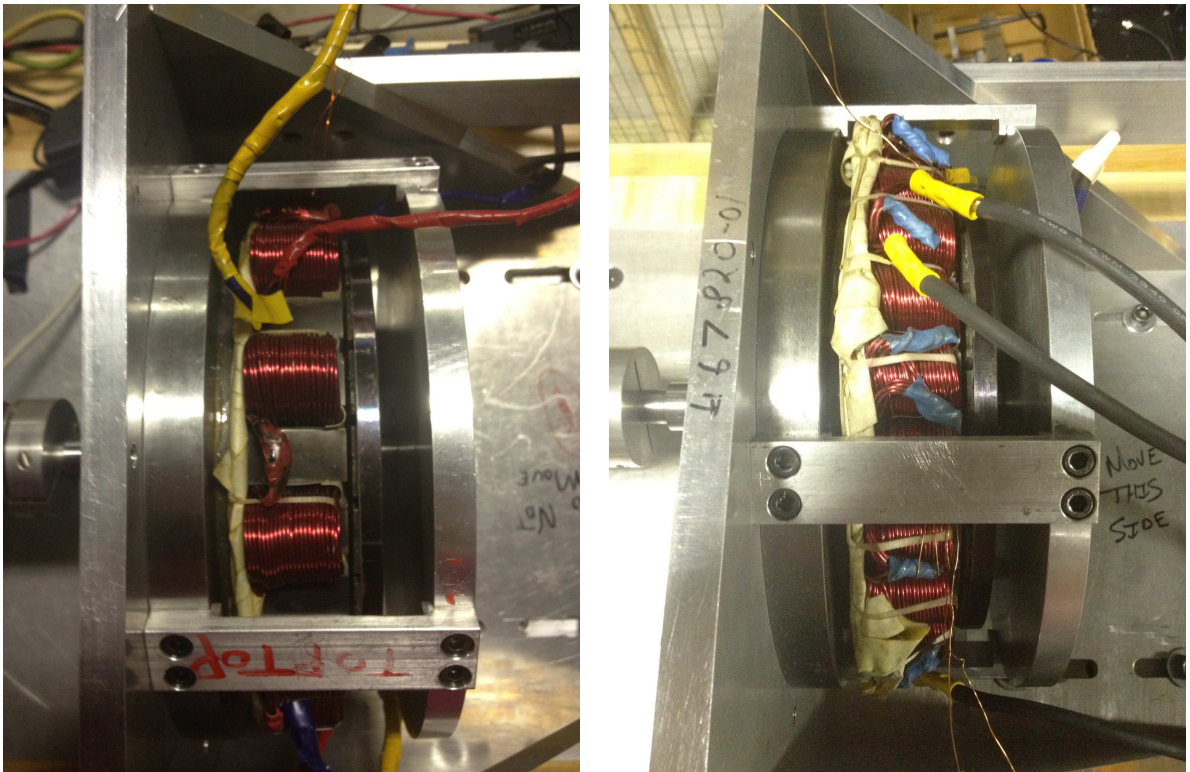


Figure 4.2: Schematic drawings of the single-sided AFPM Machines



(a) Single layer winding AFPM

(b) Double layer winding AFPM

Figure 4.3: Single-sided AFPM machines for experiment

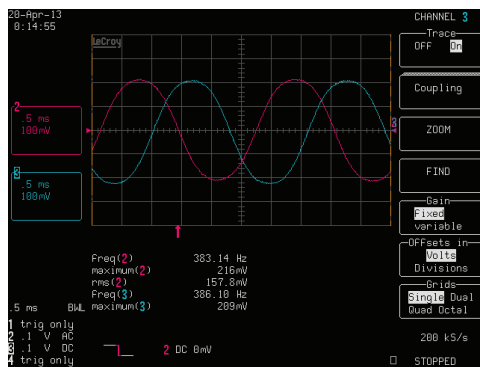
average air gap in the double layer one is 1.78 mm.



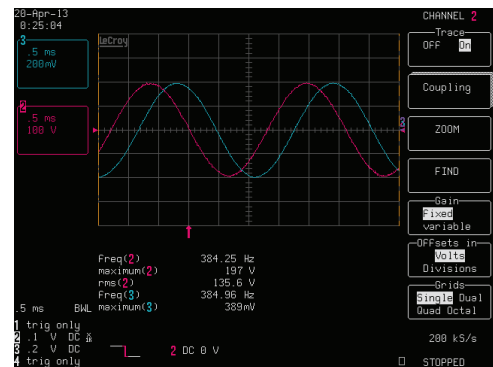
## 4.3 Machine Parameters

### 4.3.1 Back EMF Constant

The designed peak value of phase voltage (line to neutral) at a rated speed of 2800 rpm is 143 V. The line to neutral voltage waveform of the double layer winding machine at 75% of rated speed is shown in the figure. The voltage probe 100mV equals to 50V, thus the peak voltage value of 216 mV is 108 V, which matches the calculated value of 107.25 V. The single layer winding one is not shown here due to space limits.

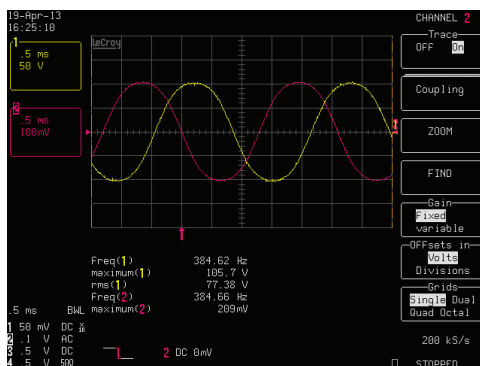


(a) Single layer winding AFPM

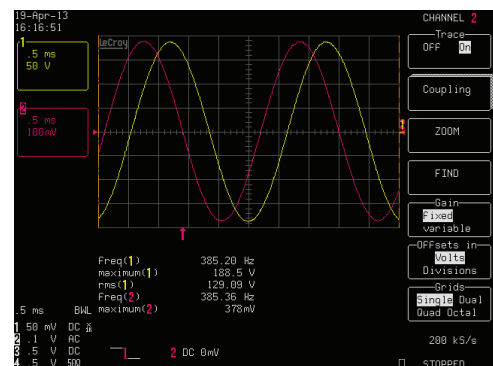


(b) Double layer winding AFPM

Figure 4.4: Single-sided AFPM machines for experiment



(a) Single layer winding AFPM



(b) Double layer winding AFPM

Figure 4.5: Single-sided AFPM machines for experiment

### 4.3.2 Resistance

The phase to neutral resistance is measured at 10A DC excitation current. The average phase resistance of a single layer winding machine is 0.049 ohm. The average phase resistance of a double layer winding machine is 0.063 ohm.

## 4.4 Test Setup

Figure 4.6 depicts the test set up.

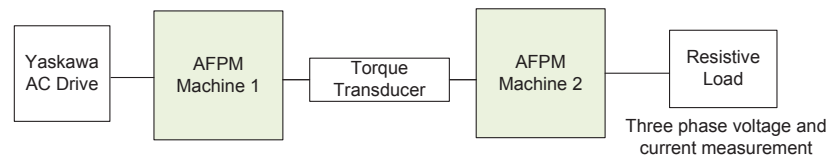


Figure 4.6: Test setup

#### 1. AC drive

The Yaskawa drive V1000 10 HP will drive one of the machines as the prime mover. Its frequency limit is 400 Hz, which means that it can only achieve 78% of rated speed. The rated speed would require 513 Hz.

#### 2. Torque transducers

For a no load test, a lower rated transducer with 2 Nm range is used for better accuracy. For a loaded test, a transducer with a larger rating 20 Nm is used. NI data acquisition DAQ 9191 is used to obtain the output voltage information from the torque transducer.

#### 3. Resistive load

The resistive load used is a variable 3.3 kW load, maximum current is 8A at Delta connections. However, in order to reach the rated output power of 6.7 kW, a large load may be used.

#### 4. Voltage and current measurements

Due to the lab limitations, three line to line voltages are measured by the Multi-meters and three phase currents are measured by the LeCory current probes.

## 4.5 Loss Analysis of the AFPM Machines

The machine power balance is:

$$P_m - P_e = P_{f+w} + P_{s,Cu} + P_{s,Fe} + P_{r,Total} \quad (4.1)$$

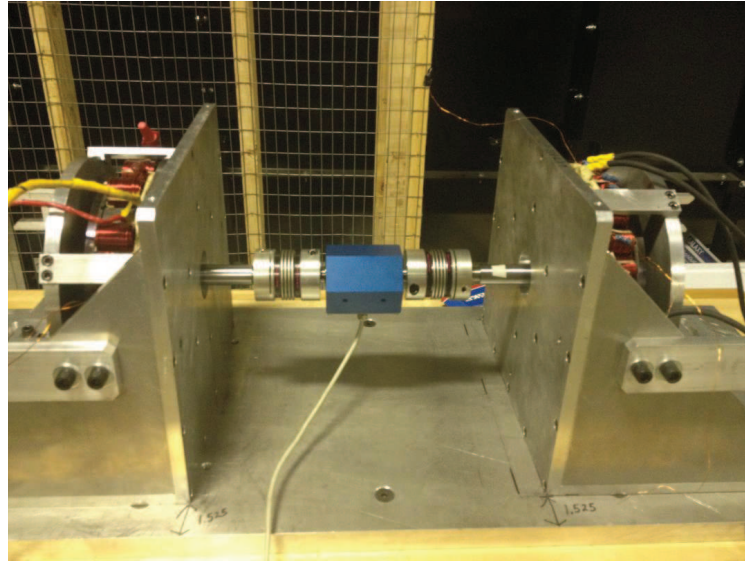
where  $P_{r,Total}$  is the total eddy current loss in both the solid rotor plate and magnets.

$P_m$  is calculated by the measured mechanical torque and speed,  $P_e$  is calculated by measuring three phase voltages and currents, and  $P_{f+w}$  is measured by the test when the stator is replaced with an uncut toroid to isolate the mechanical loss.  $P_{s,Cu}$  is calculated by the resistance and currents, and  $P_{s,Fe}$  is estimated through stator core loss measurement. Thus the eddy current loss  $P_{r,Total}$  could be isolated from the measured overall loss which equals to  $P_m - P_e$ . It should be noted that in the experiment, the eddy current loss in the solid rotor plate only and in the permanent magnets only cannot be separated.

## 4.6 Description of Tests

### 4.6.1 Test 1: Isolate the Bearing Friction Loss

In order to isolate the bearing and windage loss, the stator is replaced by an uncut toroid, which has the same overall dimensions as the wound and slotted stator. The 'machine' is assembled in the same way as previously described. For the purpose of ensuring that the bearing friction loss in the "machine" is the same as the bearing



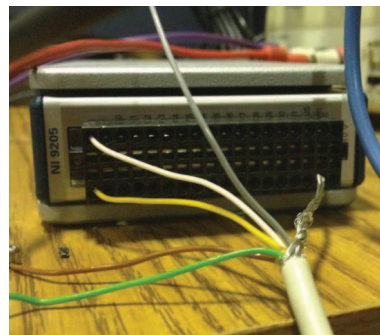
(a) Machine setup



(b) Yaskawa AC drive



(c) 3.3 kW variable resistive load



(d) NI DAQ



(e) Torque transducers

Figure 4.7: Equipments for the experiment

friction loss in the actual machine, the axial force between the uncut toroid and the rotor plate should be the same as the one between the actual stator, which has windings in it, and the rotor plate. Through FEA simulation, the air gap needs to be increased to 2.25 mm by adding more shims for equivalent axial force. By magnetostatic solver, the axial force is 2856 newton. Thus, the measured mechanical power input into this “machine” will be entirely the bearing and windage loss.

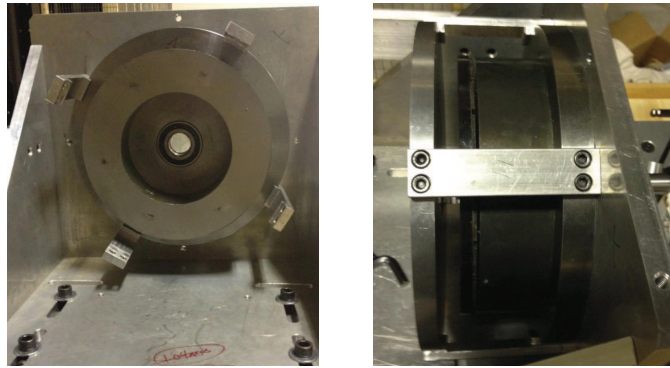


Figure 4.8: “Machine” with a uncut stator

The bearing loss at various speeds from 30 %, 40%, 50%, 75% of the rated speed are shown as:

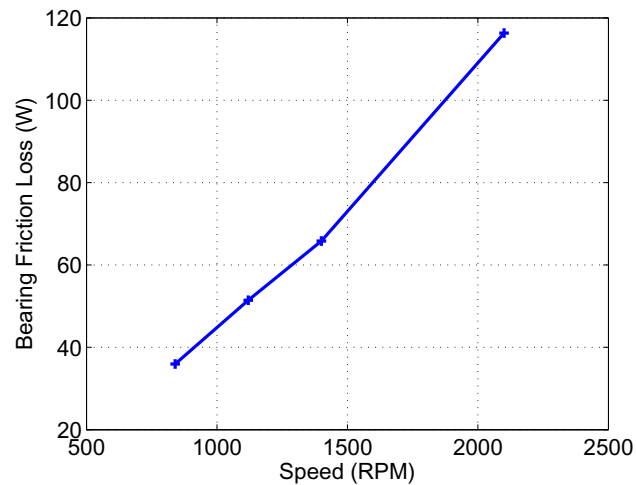


Figure 4.9: Bearing and windage loss  $P_{f+w}$  results

### 4.6.2 Test 2: Isolate the Stator Core Loss

The stator core loss is calculated by:

$$P_{s,Fe} = \text{SpecificCoreLossInTeethOnly}(f, B_{teeth}) * W_{teeth} + \\ \text{SpecificCoreLossInBackIronOnly}(f, B_{backiron}) * W_{backiron}$$

in which,  $W_{teeth}$ ,  $W_{backiron}$  is the weight of the teeth and stator back iron

The specific core loss data is measured by the methods in [77]. The specific core loss in teeth is remeasured at different conditions when only 1 tooth is excited, 4 teeth are excited and 12 teeth are excited, in order to ensure the methods are correct and to obtain the most accurate core loss. The flux density in the tooth  $B_{teeth}$  is measured by the sensing coil around one tooth in the machine as shown. The flux density in the back iron is accessed by the ratio of  $B_{backiron}/B_{teeth}$ , which is 0.65 according to 3D FEA.

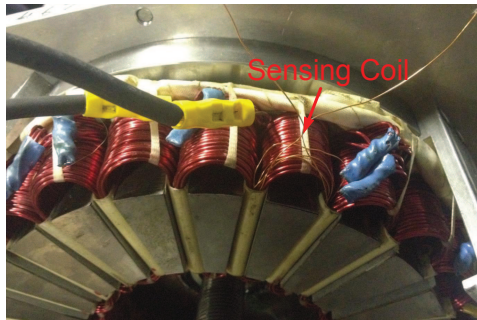


Figure 4.10: Sensing coil in the stator

### 4.6.3 Test 3: No Load Tests

The rotor and magnet loss due to stator slotting is measured through no load tests.

$$P_{Loss,No\ load} = P_{f+w} + P_{s,Fe,no\ load} + P_{r,Slot} \quad (4.2)$$

$P_{s,Fe,noload}$  is calculated as in Test 2. The flux density in the teeth is measured through the sense coil voltage as shown in Fig.4.11. It shows that the flux density in the teeth almost keeps constant, around 1.05 T. Thus,  $P_{r,Slot}$  could be separated.

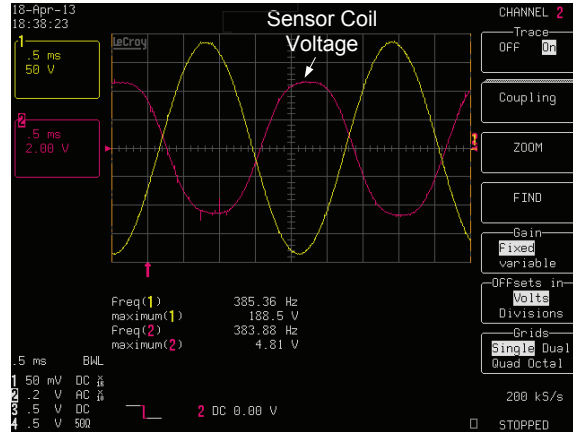


Figure 4.11: Sensing coil voltage at no load condition

The no load loss in SL and DL machine should be the same since there are no currents as shown in the blue and black line. The test loss separation results are shown in Fig. 4.12.

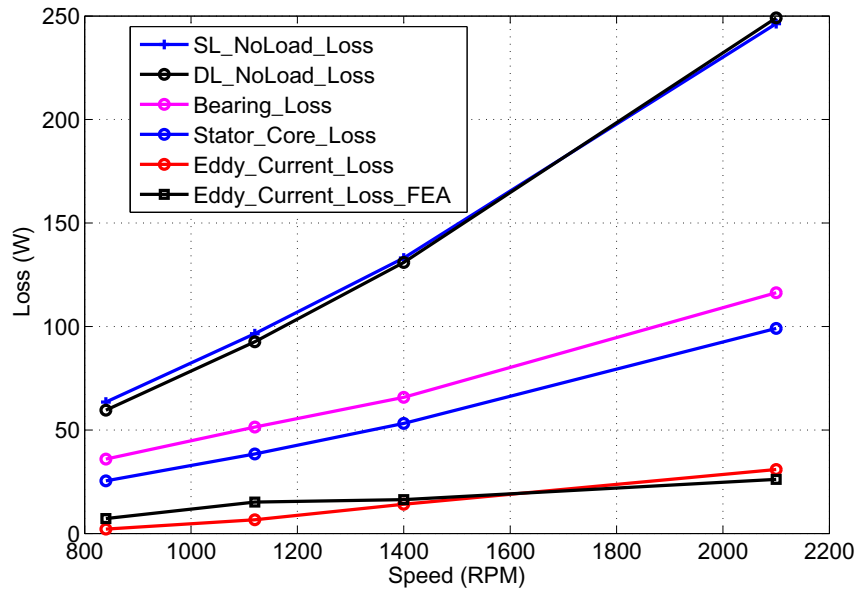


Figure 4.12: Loss separation results at no load condition

#### 4.6.4 Test 4: Load Test

The rotor and magnet loss due to both stator slotting and MMF harmonics  $P_{r,total}$  is measured through load tests.

$$P_{mech} - P_{elec} = P_{bearing} + P_{s,Cu} + P_{s,Fe} + P_{r,total} \quad (4.3)$$

##### 4.6.4.1 Double Layer Winding

Load tests are performed at 40%, 50%, 60%, 70%, and 75% of the rated speed at current of 6A (rms) . The input mechanical power  $P_{mech}$ , output electrical power  $P_{elec}$  and efficiencies are shown in Fig. 4.13.

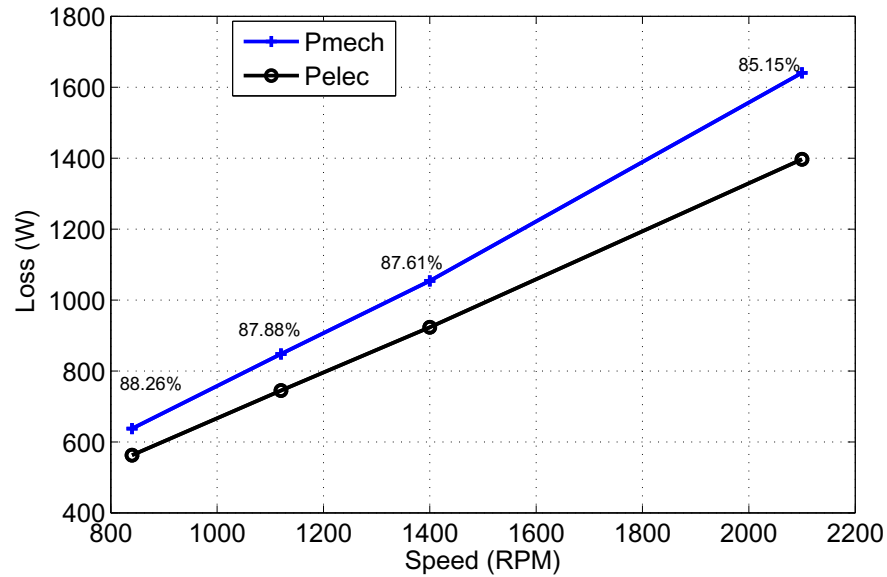


Figure 4.13: Test results for double layer winding at 6A (rms)

The total rotor eddy current loss  $P_{r,Total}$  could be obtained as shown in Fig. 4.14.



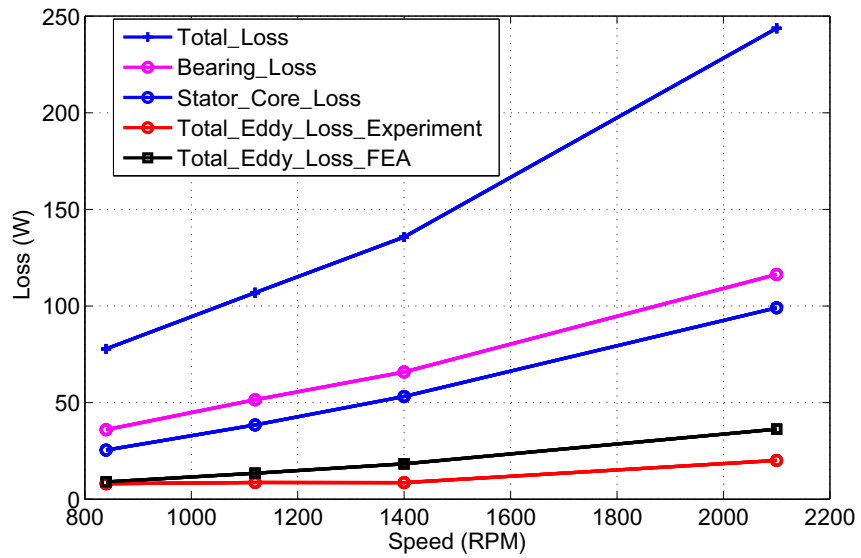


Figure 4.14: Loss separation results for double layer winding at 6A (rms)

#### 4.6.4.2 Single Layer Winding

Similarly, load tests are performed at 40%, 50%, 60%, 70%, and 75% of the rated speed at current of 6A (rms) . The results are shown in Fig. 4.15 and Fig. 4.16.

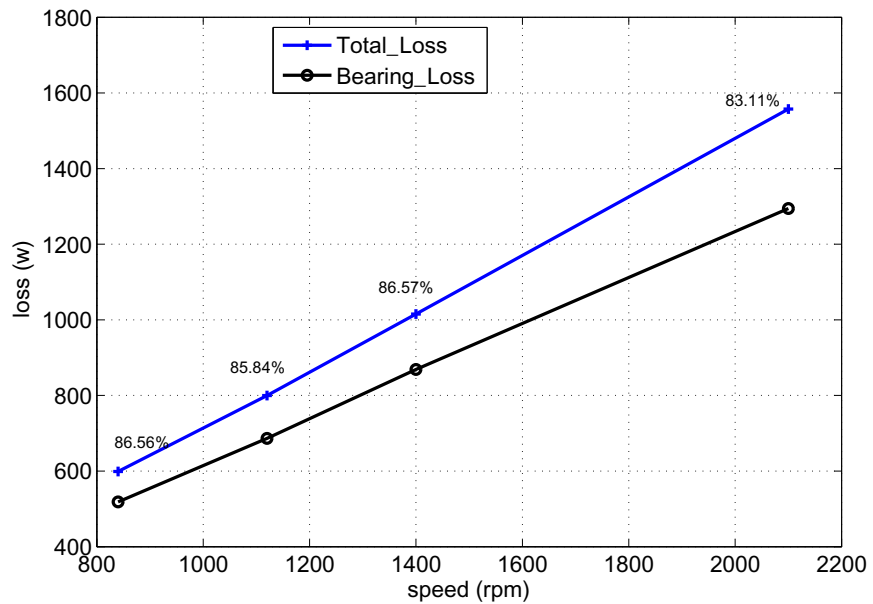


Figure 4.15: Test results for single layer winding at 6A (rms)

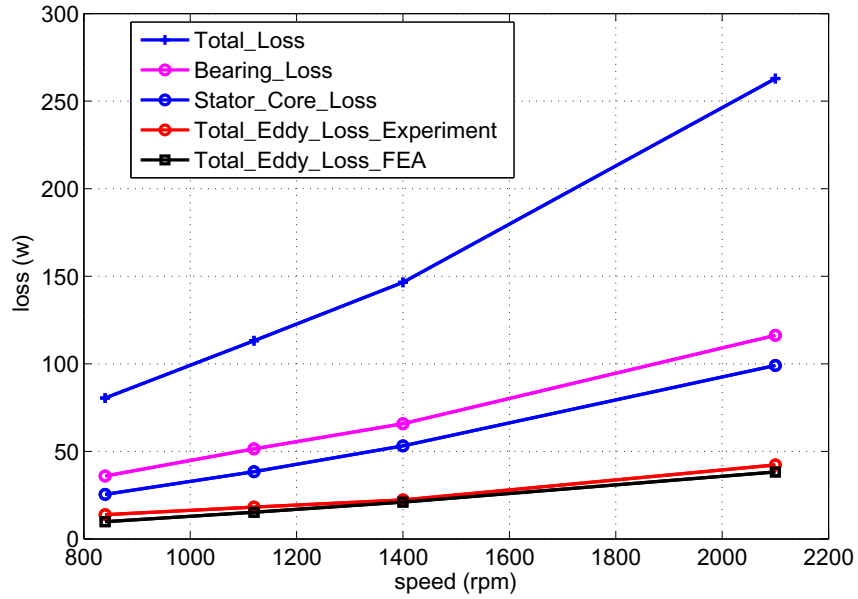


Figure 4.16: Loss separation results for single layer winding at 6A (rms)

Due to resistive load limitations, the rated current condition may not be reached at this time.

#### 4.6.5 Comparison of the Eddy Current Loss Experiment Results and FEA Simulation Results

From Fig. 4.14 , Fig. 4.14 and Fig. 4.16, it could be seen that there are some differences between 3D FEA and experimental results. It may be due to several reasons, may due to inaccuracy of measuring stator core loss.

### 4.7 Summary and Possible Future Work

Two prototype machines are assembled and tested. Methods of loss segregation are illustrated. Experiment measurements show that eddy current loss in SL machine are

higher than in DL machine. It could also be seen that bearing loss accounts for a large portion of total loss. Three dimensional FEA results are compared with experimental results from experiments.

Due to the drive frequency limit of 400 Hz and resistive load bank power limit, the test could not reach the rated condition of 6.7 kW. If possible, the machine should be tested with rated condition in the future.

## Chapter 5

# Optimal Design of an Axial Flux PM Machine

### 5.1 Introduction

The target machine for this study is a 6.7 kW, single-sided double layer NOW AFPM with 24 slots and 22 poles. This machine is used as an integrated starter-alternator for hybrid vehicles. However, this design was based on some analytical sizing equations. The design parameters and machine performances are not optimized. The purpose of this study is to provide an automatic optimal machine design approach. A multi-objective differential evolution optimization is implemented. The objectives could be loss, cost, efficiency, torque, etc. Here, maximum torque and efficiency are the goals. The optimized design is compared with the initial design of the prototype machine.

## 5.2 FEA Model of the Machine

Ideally the FEA model should be in 3D to better evaluate performance, however, due to the computation time, a 2D model is used in the optimal design with transient solution as shown in Fig. 5.1.

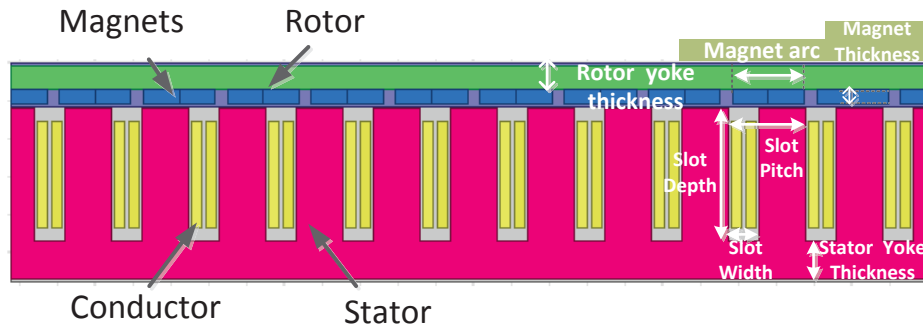


Figure 5.1: 2D FEA model of a single-sided double layer NOW 24 slots/ 22 poles AFPM

## 5.3 Design Variables

The geometry parameters are shown as in Table 1 :

|    | Variables                       | Range      | Unit |
|----|---------------------------------|------------|------|
| x1 | Slot Depth                      | [25, 40]   | mm   |
| x2 | Slot Width to Slot Pitch Ratio  | [0.3, 0.8] |      |
| x3 | Stator Yoke Thickness           | [8, 20]    | mm   |
| x4 | Magnet Thickness                | [3, 5]     | mm   |
| x5 | Magnet Span to Pole Pitch Ratio | [0.5, 0.9] |      |
| x6 | Rotor Yoke Thickness            | [5, 10]    | mm   |
| x7 | Split Ratio                     | [0.5, 0.7] |      |

Table 5.1: Design Variables and Ranges

## 5.4 Design Constrains

There are geometry constrains and operating limits as shown in Table 5.2.

The stator outer diameter is fixed at 196 mm which is usually the case due to space limitations. The air gap length is fixed at 1 mm since a slight adjustment of the air gap will result in a significant difference in machine performance, which makes it difficult to evaluate the impact of other parameters.

Current density is fixed at  $4.1 \text{ A/mm}^2$  due to cooling requirements, which is also the same as the reference machine. The maximum stator tooth and back iron flux is 1.5 T. The material properties can be changeable and included in the optimal design. However, here the materials types are fixed as the electrical steel type is M19-29G. The permanent magnet material is NdFeB 40H with the residual induction  $B_r=1.26\text{T}$ .

| Variables                     | Value | Unit            |
|-------------------------------|-------|-----------------|
| Number of slots               | 24    | -               |
| Number of poles               | 22    | -               |
| Stator outer diameter         | 196   | mm              |
| Air gap length                | 1     | mm              |
| Slot fill factor              | 0.4   | -               |
| Current density               | 4.1   | $\text{A/mm}^2$ |
| Maximum stator tooth flux     | 1.5   | T               |
| Maximum stator back iron flux | 1.5   | T               |

Table 5.2: Design Constrains

## 5.5 Design Objectives

The purpose of the optimal design is to design a machine with high torque density and high efficiency with a minimum torque requirement of 22.8 Nm to guarantee the 6700 W output power.

A multi-objective optimization algorithm is implemented. The objectives are to maximize the output torque density (Nm/kg) and efficiency:

$$\begin{aligned} \text{maximize :} f1 &= \frac{T_{em}}{W_{Copper} + W_{Steel} + W_{Magnets}} \\ \text{maximize :} f2 &= \frac{P_{output}}{P_{output} + P_{statorcoreloss} + P_{rotorPMloss} + P_{copperloss}} \end{aligned} \quad (5.1)$$

in which,  $W_{Copper}$ ,  $W_{Steel}$ ,  $W_{Magnets}$  are the weight of used copper, steel and magnets. They are calculated by volume multiplied by the density.  $P_{statorcoreloss}$  is the stator core loss,  $P_{rotorPMloss}$  is the eddy current loss in rotor back iron and magnets, and  $P_{copperloss}$  is the copper loss, mechanical losses are not considered.

Once the Pareto front is obtained, the designer can select the best design one which is a reasonable compromise between different objectives.

## 5.6 Optimization Process

Fig. 5.2 shows the flowchart of the optimal design. The FEA model is in Maxwell. MATLAB is interfaced with Maxwell to change the input parameters and postprocessing of the simulation data. A differential evolution algorithm is selected as the optimal algorithm. First an initial input parameter is generated in MATLAB, and the value is passed the value into the Maxwell FEA parametric model. The machine geometry is redrawn automatically. After the simulation in Maxwell is completed, the output parameters such as torque, loss will be exported to MATLAB. Fitness function will be calculated. If the machine performance does not meet the requirement, the differential evolution algorithm will generate the next design parameters. The process will be repeated.

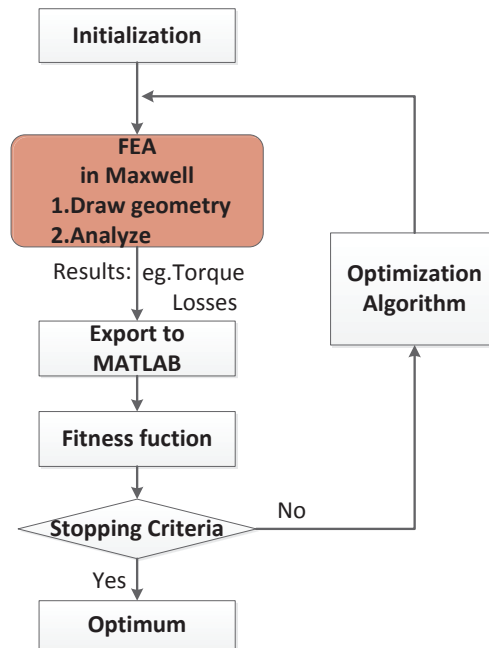


Figure 5.2: Flowchart of optimization with MATLAB/Maxwell

## 5.7 Optimization Results

The population size for the differential evolution is 40, the generation size is 20, which leads to a total 800 design. Cr is 0.9426, Fr is 0.6607. The simulation time is 25 hours in a single computer. Figure 8 shows the optimization results and the plotted Pareto front.

### 5.7.1 Compare with Initial Design

One optimization M1 is selected for the design as the blue dot in Fig. 5.3. The purple circle is the reference initial machine. It can be seen that both the torque density and efficiency is improved.



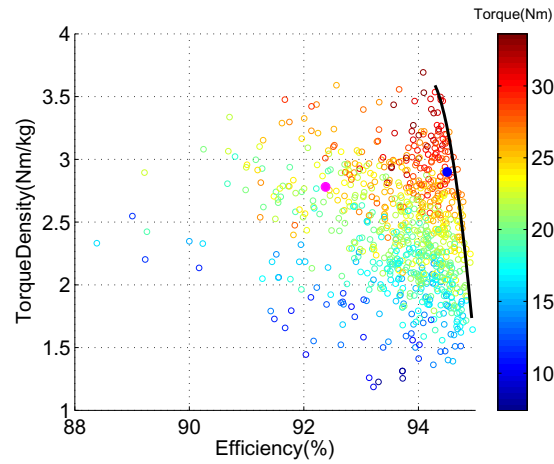


Figure 5.3: Pareto front

| Variables Compare   |                                | Initial Design | Optimized-M1 | Unit  |
|---------------------|--------------------------------|----------------|--------------|-------|
| x1                  | Slot Depth                     | 35             | 40           | mm    |
| x2                  | Slot Width to Slot Pitch Ratio | 0.3918         | 0.5149       | -     |
|                     | Slot Width                     | 8              | 10           | mm    |
| x3                  | Stator Yoke Thickness          | 10             | 14.81        | mm    |
| x4                  | Magnet Thickness               | 4              | 5.0          | mm    |
| x5                  | Magnet Arc                     | 14             | 9            | deg   |
| x6                  | Rotor Yoke Thickness           | 6              | 5.49         | mm    |
| x7                  | Split Ratio                    | 0.5918         | 0.5257       | -     |
|                     | Stator Inner Diameter          | 116            | 103          | mm    |
| Performance Compare |                                | Initial Design | Optimized-M1 | Unit  |
|                     | Torque Density                 | 2.78           | 2.9          | Nm/kg |
|                     | Efficiency                     | 92.38 %        | 94.50 %      | -     |
|                     | Max Tooth Flux                 | 1.33           | 1.34         | T     |
|                     | Max Back Iron Flux             | 1.07           | 0.7172       | T     |
|                     | Output Torque                  | 23             | 29           | Nm    |

Table 5.3: Optimization Results

### 5.7.2 Parameter Profile

Fig. 5.4 shows the input and output results as Generation=1 and 20. It could be seen that as the generation number increase, the results will be more close to the Pareto front. Fig. 5.5 and Fig. 5.6 show the relationship between the each input parameter and the output parameter.

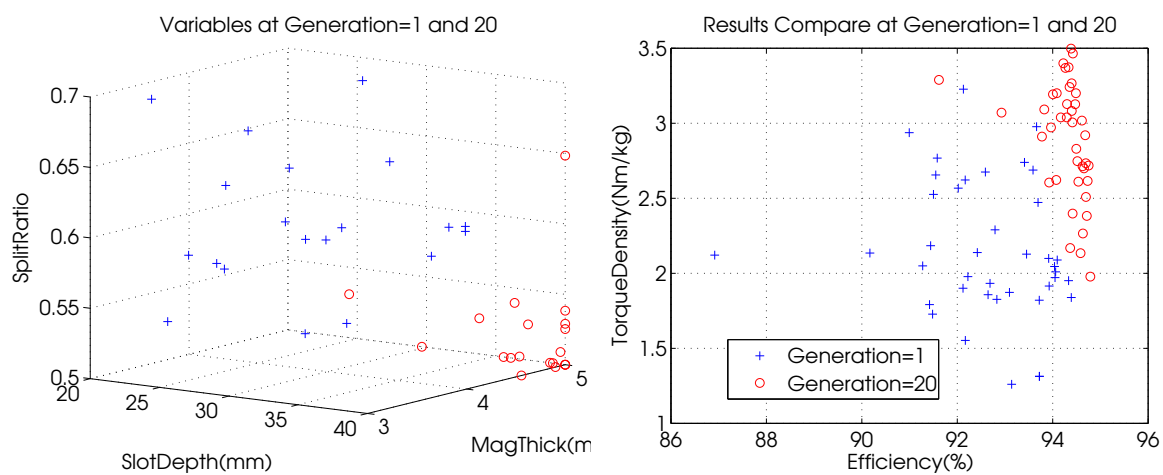


Figure 5.4: Optimization results

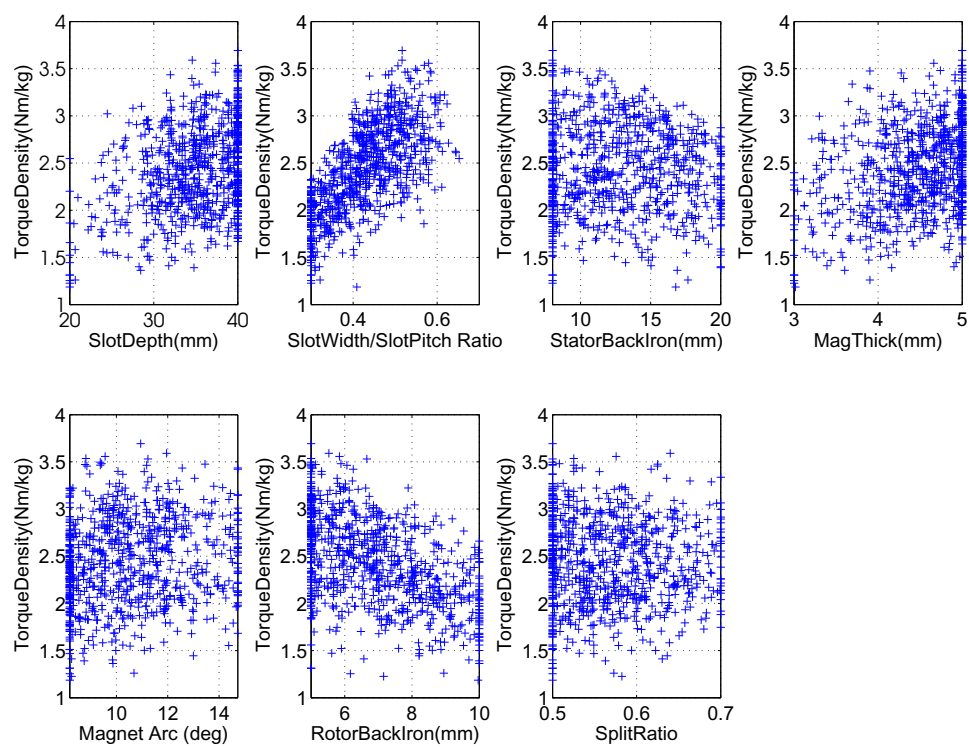


Figure 5.5: Variables vs TorqueDensity

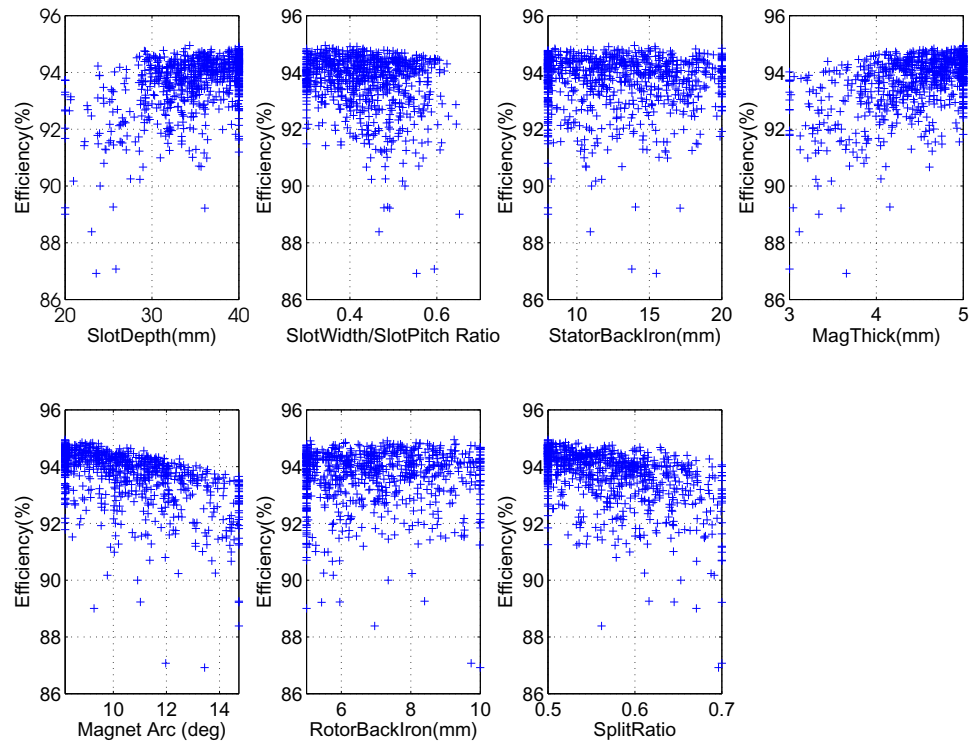


Figure 5.6: Variables vs Efficiency

### 5.7.3 Discussions

Here are some comments regarding the optimization.

In an ideal situation, we might run more generations and get more optimal solution sets. Considering the time constraints, this run only implements an 800 design, using 25 hours on a single lab computer. Also the input parameters relationship with the output parameters may be analyzed by some statistic tools.

It should be noted that this optimization focuses on only one type of axial flux machine. It is not compared with other types, such as the Torus AFPM or radial flux, etc.

The machine is optimized with fixed slot/pole numbers. The broad concept of

an “optimized machine” should include different slot/pole combinations. However, the difficulty in including the slot number and pole number as variables is that, the machine winding, excitation and boundary conditions setting would be different in the FEA model, where it is not easy to define them automatically. But it would be possible, with KOIL software used to design the winding of rotating electric machinery automatically by Luigi 2012.

The materials properties can be set as variables. It would not be difficult. Here only a few material properties are available, especially for core loss data, which is fixed in the design practice.

To further extend the overall machine design process, the optimization of a machine should be a co-simulation combined with electromagnetic as well as thermal considerations.

## 5.8 Summary

In this chapter, an automatic optimal machine design approach is presented. The FEA models used for evaluating the machine performance are surveyed. Different magnetostatic models are summarized and compared with a transient solution. Optimization methods used in the machine design are compared. It shows that a differential evolution algorithm is superior to other algorithms. Finally, an optimized design of a 24 slot/22 pole single-sided axial flux machine is illustrated with 2D transient FEA model in Maxwell and in MATLAB. Further works with various slot/pole combinations, different material types and different machine types, could be included in the automatic design process extended to a broad optimization design.

## Chapter 6

# Summary and Continue Work

In this dissertation, the focus of the work is the FEA simulation and experimental validation of solid rotor and magnet eddy current loss in single-sided axial flux permanent magnet machines.

Firstly, a detailed 2D and 3D model for eddy current loss calculation is established. From the 2D and 3D FEA simulation results comparison, it could be seen that the 2D results are not accurate. Thus 3D FEA is mainly used. This shows that at rated conditions in SL winding, the eddy current loss is mainly due to MMF space harmonics, and that eddy current loss is mostly in the solid rotor plate rather than in the magnets. In DL winding, the eddy current loss due to stator slotting and loss due to MMF space harmonics are closer and the loss in the solid rotor plate and in the magnet are almost equal.

Secondly, methods are proposed to measure the core loss in the back iron and in the teeth of a fabricated stator of a single-sided AFPM. FEA simulations are implemented, together with the measured total loss, to obtain the specific core loss data in the back iron only and in the teeth only. It is shown that during the three methods of measuring the specific core loss in teeth only, the most accurate results

can be obtained when all teeth in the machine are excited with the same current and alternating flux. The core loss in the teeth is about 1.6 times of that in the back iron averagely.

Two prototype machine, one with single layer winding and one with double layer winding are assembled and tested. During the assembly process, the attractive force between the stator and rotor needs to be taken care of. The rotor plate needs to be introduced to the stator gradually to maintain an even airgap. A proper bearing should also be selected to carry the large axial load. During the tests, methods of loss segregation are illustrated. Experimental measurements show that eddy current loss in the SL machine is higher than in the DL machine as expected. It could also be seen that bearing loss accounts for a large portion of total loss. Three dimensional FEA results are compared with experimental results from experiments. However, there is some difference. There are several possible reasons. It may be due to inaccuracy of calculating stator core loss by the data obtained when only one tooth excited. In the experiments, we were trying to limit the errors and make the measurement as accurate as possible.

For the possible future experimental work, the load test may extend to more operation points with different speeds and load conditions, particularly at the rated conditions.

Lastly, additional work about the design optimization is included. An automatic optimal machine design approach is presented. An optimized design of a 24 slot/22 pole single-sided axial flux machine is illustrated using a 2D transient FEA model in Maxwell controlled by MATLAB. Further work with various slot/pole combinations, different material types and different machine types, could be included in the automatic design process extended to a broad optimization design.

# Bibliography

- [1] D. Patterson, J. Colton, B. Mularcik, B. Kennedy, S. Camilleri, and R. Rohoza, “A comparison of radial and axial flux structures in electrical machines,” in *Electric Machines and Drives Conference, 2009. IEMDC '09. IEEE International*, 2009, pp. 1029–1035.
- [2] T.-S. Kwon, S.-K. Sul, L. Alberti, and N. Bianchi, “Design and control of an axial-flux machine for a wide flux-weakening operation region,” *Industry Applications, IEEE Transactions on*, vol. 45, no. 4, pp. 1258–1266, July-Aug. 2009.
- [3] L. Alberti, E. Fornasiero, N. Bianchi, and S. Bolognani, “Impact of rotor losses in a 12-slot 10-pole axial flux pm machine,” in *Industry Applications Society Annual Meeting, 2008. IAS '08. IEEE*, Oct. 2008, pp. 1–8.
- [4] L. Alberti, E. Fornasiero, N. Bianchi, and S. Bolognani, “Rotor losses measurements in an axial flux permanent magnet machine,” vol. 26, no. 2, June 2011, pp. 639–645.
- [5] R. Di Stefano and F. Marignetti, “Electromagnetic analysis of axial-flux permanent magnet synchronous machines with fractional windings with experimental validation,” *Industrial Electronics, IEEE Transactions on*, vol. 59, no. 6, pp. 2573–2582, 2012.

- [6] F. Caricchi, F. Maradei, G. De Donato, and F. Capponi, “Axial-flux permanent-magnet generator for induction heating gensets,” *Industrial Electronics, IEEE Transactions on*, vol. 57, no. 1, pp. 128–137, Jan. 2010.
- [7] M. Kamper, R.-J. Wang, and F. Rossouw, “Analysis and performance of axial flux permanent-magnet machine with air-cored nonoverlapping concentrated stator windings,” *Industry Applications, IEEE Transactions on*, vol. 44, no. 5, pp. 1495–1504, Sept.-Oct. 2008.
- [8] A. EL-Refaie, “Fractional-slot concentrated-windings synchronous permanent magnet machines: Opportunities and challenges,” *Industrial Electronics, IEEE Transactions on*, vol. 57, no. 1, pp. 107–121, Jan. 2010.
- [9] N. Bianchi, S. Bolognani, M. Pre, and G. Grezzani, “Design considerations for fractional-slot winding configurations of synchronous machines,” *Industry Applications, IEEE Transactions on*, vol. 42, no. 4, pp. 997–1006, July-Aug. 2006.
- [10] N. Bianchi and M. Dai Pre, “Use of the star of slots in designing fractional-slot single-layer synchronous motors,” *Electric Power Applications, IEE Proceedings* -, vol. 153, no. 3, pp. 459–466, May 2006.
- [11] E. Fornasiero, L. Alberti, N. Bianchi, and S. Bolognani, “Considerations on selecting fractional slot windings,” in *Energy Conversion Congress and Exposition (ECCE), 2010 IEEE*, 2010, pp. 1376–1383.
- [12] L. Alberti and N. Bianchi, “Theory and design of fractional-slot multilayer windings,” in *Energy Conversion Congress and Exposition (ECCE), 2011 IEEE*, 2011, pp. 3112–3119.



- [13] A. Jassal, H. Polinder, and J. A. Ferreira, “Literature survey of eddy-current loss analysis in rotating electrical machines,” *Electric Power Applications, IET*, vol. 6, no. 9, pp. 743–752, 2012.
- [14] N. Bianchi, S. Bolognani, and E. Fornasiero, “A general approach to determine the rotor losses in three-phase fractional-slot pm machines,” in *Electric Machines Drives Conference, 2007. IEMDC '07. IEEE International*, vol. 1, May 2007, pp. 634–641.
- [15] N. Bianchi, S. Bolognani, and E. Fornasiero, “An overview of rotor losses determination in three-phase fractional-slot pm machines,” *Industry Applications, IEEE Transactions on*, vol. 46, no. 6, pp. 2338–2345, nov.-dec. 2010.
- [16] N. Bianchi and E. **Fornasiero**, “Impact of mmf space harmonic on rotor losses in fractional-slot permanent-magnet machines,” *Energy Conversion, IEEE Transactions on*, vol. 24, no. 2, pp. 323–328, June 2009.
- [17] E. Fornasiero, N. Bianchi, and S. Bolognani, “Slot harmonic impact on rotor losses in fractional-slot permanent-magnet machines,” *Industrial Electronics, IEEE Transactions on*, vol. 59, no. 6, pp. 2557–2564, 2012.
- [18] L. Alberti, E. Fornasiero, and N. Bianchi, “Impact of the rotor yoke geometry on rotor losses in permanent-magnet machines,” *Industry Applications, IEEE Transactions on*, vol. 48, no. 1, pp. 98–105, 2012.
- [19] H. Polinder, M. Hoeijmakers, and M. Scuotto, “Eddy-current losses in the solid back-iron of pm machines for different concentrated fractional pitch windings,” in *Electric Machines Drives Conference, 2007. IEMDC '07. IEEE International*, vol. 1, May 2007, pp. 652–657.

- [20] H. Polinder, M. Hoeijmakers, and M. Scuotto, “Eddy-current losses in the solid back-iron of permanent-magnet machines with concentrated fractional pitch windings,” in *Power Electronics, Machines and Drives, 2006. The 3rd IET International Conference on*, 2006, pp. 479–483.
- [21] P. Lawrenson, P. Reece, and M. Ralph, “Tooth-ripple losses in solid poles,” *Electrical Engineers, Proceedings of the Institution of*, vol. 113, no. 4, pp. 657–662, 1966.
- [22] A. Jassal, H. Polinder, D. Lahaye, and J. Ferreira, “Analytical and fe calculation of eddy-current losses in pm concentrated winding machines for wind turbines,” in *Electric Machines Drives Conference (IEMDC), 2011 IEEE International*, May 2011, pp. 717 –722.
- [23] A. Jassal, H. Polinder, D. Lahaye, and J. Ferreira, “Comparison of analytical and finite element calculation of eddy-current losses in pm machines,” in *Electrical Machines (ICEM), 2010 XIX International Conference on*, Sept. 2010, pp. 1 –7.
- [24] M. Firmansyah, A. Jassal, H. Polinder, and D. Lahaye, “Eddy current loss calculation in rotor back iron for concentrated winding pm generator,” in *Electrical Machines (ICEM), 2012 XXth International Conference on*, 2012, pp. 2666–2670.
- [25] R. Nuscheler, “Two-dimensional analytical model for eddy-current rotor loss calculation of pms machines with concentrated stator windings and a conductive shield for the magnets,” in *Electrical Machines (ICEM), 2010 XIX International Conference on*, Sept. 2010, pp. 1 –6.
- [26] B. Aslan, E. Semail, and J. Legranger, “Analytical model of magnet eddy-current volume losses in multi-phase pm machines with concentrated winding,” in *Energy Conversion Congress and Exposition (ECCE), 2012 IEEE*, 2012, pp. 3371–3378.

- [27] L. J. Wu, Z. Zhu, D. Staton, M. Popescu, and D. Hawkins, “Analytical modeling and analysis of open-circuit magnet loss in surface-mounted permanent-magnet machines,” *Magnetics, IEEE Transactions on*, vol. 48, no. 3, pp. 1234–1247, 2012.
- [28] P. Zhang, G. Sizov, J. He, D. Ionel, and N. Demerdash, “Calculation of magnet losses in concentrated-winding permanent magnet synchronous machines using a computationally efficient - finite element method,” in *Energy Conversion Congress and Exposition (ECCE), 2012 IEEE*, 2012, pp. 3363–3370.
- [29] Z. Zhu, K. Ng, N. Schofield, and D. Howe, “Analytical prediction of rotor eddy current loss in brushless machines equipped with surface-mounted permanent magnets. ii. accounting for eddy current reaction field,” in *Electrical Machines and Systems, 2001. ICEMS 2001. Proceedings of the Fifth International Conference on*, vol. 2, 2001, pp. 810–813 vol.2.
- [30] Z. Zhu, K. Ng, N. Schofield, and D. Howe, “Improved analytical modelling of rotor eddy current loss in brushless machines equipped with surface-mounted permanent magnets,” *Electric Power Applications, IEE Proceedings -*, vol. 151, no. 6, pp. 641 – 650, nov. 2004.
- [31] D. Ishak, Z. Zhu, and D. Howe, “Eddy-current loss in the rotor magnets of permanent-magnet brushless machines having a fractional number of slots per pole,” *Magnetics, IEEE Transactions on*, vol. 41, no. 9, pp. 2462 – 2469, Sept. 2005.
- [32] Z. X. Fang, Z. Q. Zhu, L. J. Wu, and Z. P. Xia, “Simple and accurate analytical estimation of slotting effect on magnet loss in fractional-slot surface-mounted pm

- machines,” in *Electrical Machines (ICEM), 2012 XXth International Conference on*, 2012, pp. 464–470.
- [33] M. Etemadrezai, J. J. Wolmarans, H. Polinder, and J. A. Ferreira, “Precise calculation and optimization of rotor eddy current losses in high speed permanent magnet machine,” in *Electrical Machines (ICEM), 2012 XXth International Conference on*, 2012, pp. 1399–1404.
- [34] G. Ugalde, Z. Zhu, J. Poza, and A. Gonzalez, “Analysis of rotor eddy current loss in fractional slot permanent magnet machine with solid rotor back-iron,” in *Electrical Machines (ICEM), 2010 XIX International Conference on*, Sept. 2010, pp. 1–6.
- [35] G. Ugalde, Z. Zhu, J. Poza, and A. Gonzalez, “Investigation of rotor eddy current losses in fractional slot pm machines with solid rotor back-iron,” in *Electrical Machines and Systems (ICEMS), 2011 International Conference on*, 2011, pp. 1–5.
- [36] A. Cavagnino, M. Lazzari, A. Miotto, A. Tenconi, and S. Vaschetto, “Impact of the rotor back-iron resistivity on the rotor eddy-current losses in fractional-slot concentrated windings pm machines,” in *Energy Conversion Congress and Exposition (ECCE), 2011 IEEE*, 2011, pp. 1604–1611.
- [37] R.-J. Wang and M. Kamper, “Calculation of eddy current loss in axial field permanent-magnet machine with coreless stator,” *Energy Conversion, IEEE Transactions on*, vol. 19, no. 3, pp. 532–538, Sept. 2004.
- [38] D. Saban and T. Lipo, “Hybrid approach for determining eddy-current losses in high-speed pm rotors,” in *Electric Machines Drives Conference, 2007. IEMDC '07. IEEE International*, vol. 1, 2007, pp. 658–661.

- [39] K. Yamazaki, Y. Fukushima, and M. Sato, “Loss analysis of permanent-magnet motors with concentrated windings variation of magnet eddy current loss due to stator and rotor shapes,” *Industry Applications, IEEE Transactions on*, vol. 45, no. 4, pp. 1334–1342, July-Aug. 2009.
- [40] L. Mthombeni and P. Pillay, “Core losses in motor laminations exposed to high-frequency or nonsinusoidal excitation,” *Industry Applications, IEEE Transactions on*, vol. 40, no. 5, pp. 1325–1332, Sept.-Oct. 2004.
- [41] M. Ibrahim and P. Pillay, “Novel equipment for the measurement of core losses in laminations for advanced machines,” in *Electric Machines Drives Conference (IEMDC), 2011 IEEE International*, May 2011, pp. 1231–1236.
- [42] P. Pillay, “Improved design of motors for increased efficiency in residential and commercial buildings,” in *Final Report, the EMERF Research Consortium on Losses in Lamination Steels, Clarkson University, Potsdam, New York, USA*, Oct 16 2008, pp. 1231–1236.
- [43] C. Steinmetz, “On the law of hysteresis,” *Proceedings of the IEEE*, vol. 72, no. 2, pp. 197–221, feb. 1984.
- [44] R. H. Pry and C. Bean, “Calculation of the energy loss in magnetic sheet materials using a domain model,” *Journal of Applied Physics*, vol. 29, no. 3, pp. 532–533, 1958.
- [45] G. Bertotti, “General properties of power losses in soft ferromagnetic materials,” *Magnetics, IEEE Transactions on*, vol. 24, no. 1, pp. 621–630, Jan 1988.

- [46] H. Shimoji, B. Borkowski, T. Todaka, and M. Enokizono, “Visualizing iron loss distribution in permanent magnet motors,” in *Electrical Machines and Systems (ICEMS), 2012 15th International Conference on*, 2012, pp. 1–5.
- [47] H. Domeki, Y. Ishihara, C. Kaido, Y. Kawase, S. Kitamura, T. Shimomura, N. Takahashi, T. Yamada, and K. Yamazaki, “Investigation of benchmark model for estimating iron loss in rotating machine,” *Magnetics, IEEE Transactions on*, vol. 40, no. 2, pp. 794 – 797, march 2004.
- [48] D. Ionel, M. Popescu, S. Dellinger, T. Miller, R. Heideman, and M. McGilp, “On the variation with flux and frequency of the core loss coefficients in electrical machines,” *Industry Applications, IEEE Transactions on*, vol. 42, no. 3, pp. 658 – 667, May-June 2006.
- [49] D. Ionel, M. Popescu, M. McGilp, T. Miller, S. Dellinger, and R. Heideman, “Computation of core losses in electrical machines using improved models for laminated steel,” *Industry Applications, IEEE Transactions on*, vol. 43, no. 6, pp. 1554 –1564, nov.-dec. 2007.
- [50] A. Clerc and A. Muetze, “Measurement of stator core magnetic degradation during the manufacturing process,” *Industry Applications, IEEE Transactions on*, vol. 48, no. 4, pp. 1344 –1352, July-Aug. 2012.
- [51] S. Sprague, “An examination of magnetic property variation of specification-acceptable electrical steel,” in *Electrical Machines (ICEM), 2012 XXth International Conference on*, Sept. 2012, pp. 1172 –1177.
- [52] A. Boglietti, A. Cavagnino, L. Ferraris, and M. Lazzari, “The annealing influence onto the magnetic and energetic properties in soft magnetic material after punch-

- ing process,” in *Electric Machines and Drives Conference, 2003. IEMDC'03. IEEE International*, vol. 1, June 2003, pp. 503 – 508 vol.1.
- [53] W. Arshad, T. Ryckebusch, F. Magnussen, H. Lendenmann, B. Eriksson, J. Soulard, and B. Malmros, “Incorporating lamination processing and component manufacturing in electrical machine design tools,” in *Industry Applications Conference, 2007. 42nd IAS Annual Meeting. Conference Record of the 2007 IEEE*, Sept. 2007, pp. 94 –102.
- [54] N. Bianchi and S. Bolognani, “Brushless dc motor design: an optimisation procedure based on genetic algorithms,” in *Electrical Machines and Drives, 1997 Eighth International Conference on (Conf. Publ. No. 444)*, sep 1997, pp. 16 –20.
- [55] N. Bianchi and S. Bolognani, “Design optimisation of electric motors by genetic algorithms,” *Electric Power Applications, IEE Proceedings -*, vol. 145, no. 5, pp. 475 –483, sep 1998.
- [56] N. Bianchi, D. Durello, and E. Fornasiero, “Multi-objective optimization of a pm assisted synchronous reluctance machine, including torque and sensorless detection capability,” *IET Conference Publications*, vol. 2012, no. CP592, pp. B34–B34, 2012. [Online]. Available: <http://link.aip.org/link/abstract/IEECPS/v2012/iCP592/pB34/s1>
- [57] N. Bianchi, D. Durello, and E. Fornasiero, “Multi-objective optimization of an interior pm motor for a high performance drive,” in *International Conference on Electrical Machines (ICEM), 2012 IEEE*, September 2-5 2012.
- [58] G. Pellegrino and F. Cupertino, “Ipm motor rotor design by means of fea-based multi-objective optimization,” in *Industrial Electronics (ISIE), 2010 IEEE International Symposium on*, July 2010, pp. 1340 –1346.

- [59] G. Pellegrino and F. Cupertino, “Fea-based multi-objective optimization of ipm motor design including rotor losses,” in *Energy Conversion Congress and Exposition (ECCE), 2010 IEEE*, Sept. 2010, pp. 3659–3666.
- [60] M. V. D. Geest, H. Polinder, J. A. Ferreira, and D. Zeilstra, “Optimization and comparison of electrical machines using particle swarm optimization,” in *International Conference on Electrical Machines (ICEM), 2012 IEEE*, September 2-5 2012.
- [61] R. Wrobel and P. Mellor, “Particle swarm optimisation for the design of brushless permanent magnet machines,” in *Industry Applications Conference, 2006. 41st IAS Annual Meeting. Conference Record of the 2006 IEEE*, vol. 4, Oct. 2006, pp. 1891–1897.
- [62] M. Balaji and V. Kamaraj, “Design optimization of switched reluctance machine using particle swarm optimization,” in *Electrical Energy Systems (ICEES), 2011 1st International Conference on*, Jan. 2011, pp. 164–169.
- [63] H. Hasaniien, “Particle swarm design optimization of transverse flux linear motor for weight reduction and improvement of thrust force,” *Industrial Electronics, IEEE Transactions on*, vol. 58, no. 9, pp. 4048–4056, Sept. 2011.
- [64] J. Gao, H. Sun, L. He, Y. Dong, and Y. Zheng, “Optimization design of switched reluctance motor based on particle swarm optimization,” in *Electrical Machines and Systems (ICEMS), 2011 International Conference on*, Aug. 2011, pp. 1–5.
- [65] Y. Duan, R. Harley, and T. Habetler, “Method for multi-objective optimized designs of surface mount permanent magnet motors with concentrated or distributed stator windings,” in *Electric Machines and Drives Conference, 2009. IEMDC '09. IEEE International*, May 2009, pp. 323–328.



- [66] D. Zarko, D. Ban, and T. Lipo, "Design optimization of interior permanent magnet (ipm) motors with maximized torque output in the entire speed range," in *Power Electronics and Applications, 2005 European Conference on*, 0-0 2005, pp. 10 pp. –P.10.
- [67] W. Ouyang, D. Zarko, and T. Lipo, "Permanent magnet machine design practice and optimization," in *Industry Applications Conference, 2006. 41st IAS Annual Meeting. Conference Record of the 2006 IEEE*, vol. 4, Oct. 2006, pp. 1905 –1911.
- [68] M. Schoning, "Automated electrical machine design with differential evolution techniques," in *Electric Drives Production Conference (EDPC), 2011 1st International*, Sept. 2011, pp. 221 –224.
- [69] G. Sizov, D. Ionel, and N. Demerdash, "Multi-objective optimization of pm ac machines using computationally efficient - fea and differential evolution," in *Electric Machines Drives Conference (IEMDC), 2011 IEEE International*, May 2011, pp. 1528 –1533.
- [70] G. Sizov, P. Zhang, D. Ionel, N. Demerdash, and M. Rosu, "Automated bi-objective design optimization of multi-mw direct-drive pm machines using ce-fea and differential evolution," in *Energy Conversion Congress and Exposition (ECCE), 2011 IEEE*, Sept. 2011, pp. 3672 –3678.
- [71] Y. Duan and D. Ionel, "A review of recent developments in electrical machine design optimization methods with a permanent magnet synchronous motor benchmark study," in *Energy Conversion Congress and Exposition (ECCE), 2011 IEEE*, Sept. 2011, pp. 3694 –3701.
- [72] Y. Duan and D. Ionel, "Non-linear scaling rules for brushless pm synchronous machines based on optimal design studies for a wide range of power ratings," in

- Energy Conversion Congress and Exposition (ECCE), 2012 IEEE*, Sept. 2012, pp. 2334–2341.
- [73] P. Zhang, G. Sizov, D. Ionel, and N. Demerdash, “Design optimization of spoke-type ferrite magnet machines by combined design of experiments and differential evolution algorithms,” in *Electric Machines Drives Conference (IEMDC), 2013 IEEE International*, 2013, pp. 892–898.
- [74] J. Colton, D. Patterson, and J. Hudgins, “Rotor losses in axial-flux permanent-magnet machines with non-overlapped windings,” in *Power Electronics, Machines and Drives (PEMD 2010), 5th IET International Conference on*, april 2010, pp. 1–6.
- [75] L. Mthombeni, P. Pillay, and R. Strnat, “A new Epstein frame for lamination core loss measurements at high frequencies and flux densities,” in *Electric Machines and Drives, 2005 IEEE International Conference on*, May 2005, pp. 597–600.
- [76] W.L. Soong, “Bh curve and iron loss measurements for magnetic materials,” *Power Engineering Briefing Note Series*, May 2008.
- [77] X. Yang, D. Patterson, and J. Hudgins, “Core loss measurement in the actual finished stator of a single-sided axial flux permanent magnet machine,” in *Electric Machines Drives Conference, 2013. IEMDC '13. IEEE International*, vol. 1, May 2013.